Mestrado Integrado em Engenharia Química

Experimental and Numerical Studies on Topology of Mixing

Tese de Mestrado

de

Margarida Sarmento e Cunha Abrunhosa de Brito

Desenvolvida no âmbito da unidade curricular de Dissertação

realizado em

LSRE – Laboratory of Separation and Reaction Engineering

Orientadores: Professor José Carlos Lopes

Doutor Ricardo Jorge Santos

Departamento de Engenharia Química

julho de 2016

"Põe quanto és no mínimo que fazes"

Fernando Pessoa

Agradecimentos

Tenho a plena consciência que sozinha nada disto seria possível.

Gostava de agradecer a todos os que estiveram presentes durante estes meses de trabalho e que fizeram com que este projeto se tornasse uma realidade.

Em primeiro lugar, aos meus orientadores, Professor José Carlos Lopes e Doutor Ricardo Santos, pelo constante incentivo, por todos os ensinamentos e pela possibilidade de poder fazer parte desta equipa, o MixingGroup.

Depois, à Professora Madalena Dias, por me ter dado a oportunidade de fazer parte do LSRE – Laboratory of Separation and Reaction Engeneering, em particular, do MixingGroup e, pela permanente disponibilidade.

Queria agradecer igualmente a todo o MixingGroup: ao Carlos Teixeira, à Gabriela Ruphuy, ao Marcelo Costa, ao Nelson Gonçalves e ao Rómulo Oliveira por todas as sugestões e ajudas durante estes meses de trabalho.

Aos meus pais e irmãos, muito obrigada por sempre me encorajarem a agarrar as oportunidades e por me ajudarem a superar cada obstáculo que a vida nos vai colocando.

Aos meus avós, a forma como sempre me apoiaram e me fizeram acreditar que poderia chegar mais longe naquilo que faço.

Por fim, agradeço aos amigos que de uma forma ou de outra ajudaram à realização desta tese.

Abstract

The initial relative location of two chemical species in a reacting flow, i.e. the initial topology of mixing, plays a key role in the mixing time and in the final outcome of complex reactions such as polymerizations. This work concerns the following topics in the influence of topology on mixing of two fluids in two rotational devices used in rheometers.

The plate/plate and cone/plate geometries used in rheometers are examples of rotational devices. The plate/plate geometry consists of two plates with the fluid placed on the narrow space between them. The upper plate rotates clockwise while the bottom plate is stationary. In the cone/plate geometry the fluid is between a stationary horizontal plate and a rotating shallow cone.

In this work the flow in these two devices is studied using 3D Computational Fluid Dynamics (CFD) simulations and the results compared with previous works. The influence of the initial topology of the fluid is examined through the simulation of two fluids with the same properties. The resulting lamellar structure is described using the scale of segregation concept.

Rheological experiments are performed in order to draw conclusions about the influence of topology of mixing for two fluids with different properties in a plate/cone rheometer. These results are again compared to the simulations.

Other studies, such as the influence of rotation and the analysis of the numerical diffusivity, are carried out using the plate/plate rotational geometry.

Keywords (Theme): Mixing, plate/plate rheometer, cone/plate rheometer, rheological tests and CFD

Resumo

A localização relativa inicial de duas espécies químicas num escoamento reacional, ou seja, a topologia inicial da mistura, desempenha um papel chave no tempo de mistura e no resultado final de reações complexas tais como polimerizações. Este trabalho centra-se na influência da topologia das misturas de dois fluidos em dois dispositivos rotacionais usados em reómetros.

As geometrias prato/prato e cone/prato usados em reómetros são exemplos de dispositivos rotacionais. A geometria prato/prato consiste em dois pratos em que o fluido ocupa o espaço entre eles. O prato de cima está a rodar no sentido horário enquanto o prato de baixo está parado. Na geometria cone/prato, o fluído está entre um prato horizontal estacionário e um cone raso que se move.

Neste trabalho, o escoamento nestes dispositivos é estudado através de simulações de Computação em Fluidos Dinâmicos (CFD) tridimensionais e os resultados comparados com trabalhos anteriores. A influência da topologia inicial dos fluidos é estudada a partir de dois fluídos com as mesmas propriedades. A estrutura lamelar resultante é descrita usando o conceito de escala de segregação.

As experiências reológicas são realizadas com o objetivo de se obter conclusões sobre a influência da topologia de mistura de dois fluidos com diferentes propriedades num reómetro cone/prato. Os resultados serão comparados com o caso simulado.

Outros estudos, tais como a influência da rotação e a análise da difusividade numérica, são realizados recorrendo a uma geometria rotacional prato/prato.

Palavras-chave (Tema): Mistura, reómetro prato/prato, reómetro cone/prato, testes reológicos e CFD

Declaração

Declaro, sob compromisso de honra, que este trabalho é original e que todas as contribuições não originais foram devidamente referenciadas com identificação da fonte.

Margarida Sarmento e Cunha Abrunhosa de Brito

Margarida Sarmento e Cunha Abrunhosa de Brito

julho de 2016

Contents

List of Figures

List of Tables

Notation

$\dot{a}$	Rate of the formation of the interface	m^2/s
C	Concentration of the chemical species	mol/m^3
$\bar{C}$	Mean concentration	mol/m^3
C_N	Courant Number	
C_p	Heat capacity	J/kg K
D	Diameter of the plate	m
D_{ef}	Diffusivity coefficient	m^2/s
D_m	Molecular diffusivity	m^2/s
D_n	Numerical diffusivity	m^2/s
h	Space between the two plates	m
$H(t)$	Heaviside function	
i	Chemical species	
I_s	Intensity of segregation	
j	Number of lamellae	
K	Thermal conductivity	W/m K
l	Length of the channel	m
L	Angular momentum	kg m^2/s
m	Mass	kg
M	Linear momentum	kg m/s
n	Number of rotations	
p	Pressure	Pa
Pe	Péclet Number	
r	Radius of plate or polar coordinate	m
R	Rate of production of a chemical species	$kg/m^3 s$
Re	Reynolds Number	
R_p	Radius of the plate	m
$R(r)$	Mean correlation coefficient	
s	Striation thickness	m
S	Rate of creation by addition from the dispersed phase	$kg/m^3 s$
S_s	Scale of segregation	
t	Time	s
T	Temperature	K
U	Velocity of the fluid in the chamber	m/s
v	Velocity	m/s
v^*	Velocity in the interface	m/s
v^I	Velocity of the fluid I	m/s
v^{II}	Velocity of the fluid II	m/s
v^{III}	Velocity of the fluid III	m/s
v^{IV}	Velocity of the fluid IV	m/s
x	Space coordinate	m
x_i	Radius of an element at time i	m
x_f	Radius of an element at time f	m
x^*	Position of the interface	
X	Initial position vector	m
y	Space coordinate	m
z	Position in z direction or space coordinate	m

Greek letters

α	Volume fraction of substance	
β	Angle between plate and cone	rad
$\dot{\gamma}$	Shear rate	s^{-1}
δ	Local thickness of a lamella	m
Δx	Edge of one element of the mesh	m
Δt	Time step	s
ζ	Torque	$N \cdot m$
θ	Position in the θ-direction or cylindrical coordinate	rad
λ	Stretch ratio	
μ	Viscosity	$Pa \cdot s$
μ_{app}	Apparent viscosity	$Pa \cdot s$
μ^I	Viscosity of the fluid I	$Pa \cdot s$
μ^{II}	Viscosity of the fluid II	$Pa \cdot s$
μ^{III}	Viscosity of the fluid III	$Pa \cdot s$
μ^{IV}	Viscosity of the fluid IV	$Pa \cdot s$
$\mu\phi_v$	Viscous dissipation	$J/m^2 kg$
v	Velocity	m/s
ρ	Density	kg/m^3
σ^2	Variance	
τ	Shear stress	N/m^2
$\tau^*_{gly/sol}$	Shear stress of the glycerol at the interface	N/m^2
$\tau^*_{sol/gly}$	Shear stress of the solution at the interface	N/m^2
φ	Spherical coordinate	
ω	Angular speed	rad/s

Indexes

0	Initial
1	Chemical species
2	Chemical species
t	Time instant
A	Chemical species
C_1	Concentration of the chemical species 1
	Final
glycerol	Chemical species
$mixt\ 2lam$	Strias with 2 lamellae
$mixt\ 3lam$	Strias with 3 lamellae
$mixt\ 4lam$	Strias with 4 lamellae
r	Radial direction in cylindrical or spherical coordinates
water	Chemical species
z	Axial direction in cylindrical or x component of the variable
θ	Circumferential direction in cylindrical or θ component of the variable in spherical coordinates
φ	φ component of the variable in spherical coordinates

List of Acronyms

3D	Three-dimensional
CIJ	Confined Impinging Jets
CFD	Computational Fluid Dynamics

FEUP   Faculty of Engineering of the University of Porto
LSRE   Laboratory of Separation and Reaction Engineering

PDEs   Partial Differential Equations
RIM   Reaction Injection Moulding
VOF   Volume-of-Fluid

1 Introduction

1.1 Motivation and Relevance

NETmix and Confined Impinging Jets – CIJs - are examples of micro or mesomixers. NETmix (Figure 1) consists of a network of interconnected channels and chambers with two dimensional geometry, developed at LSRE-LCM and patented by FEUP (Laranjeira, Lopes, and Dias 2009, Lopes et al. 2013). On the other hand, CIJs (Figure 2) are used in Reaction Injection Moulding – RIM – which is an industrial application of an opposed jets mixer, i.e., T-jets, which consists on the impingement of two fluids streams of reactants in a confined chamber (Fonte 2012).
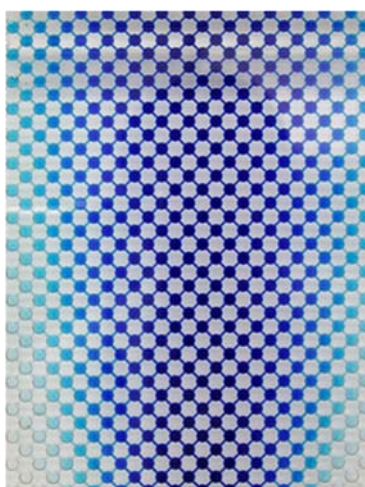
Figure 1 Mesostructured network reactor - NETmix

Figure 2 T-jets mixer

Typically, these devices operate in transitional regimes, which are generally non-isotropic flows. As this flow has a predominant direction for shearing, the initial topology, i.e., the initial position of a reactant in relation to other, plays a major role on the evolution of mixing scales.

As the influence of the topology is an unexplored topic, the topology studies of mixing are made using well-defined flows as those occurring in rotational devices used in rheometry. A rheometer is a laboratory device where the fluid is deformed by shearing and a pure shear flow is generated creating adjacent layers of fluid which slide over each other with different speeds.

In this work, the flow in two rheometer configurations, plate/plate and cone/plate, are studied. These types of flow enable to set quite homogenous mixing scales throughout the flow domain being particularly useful for generating chemical reaction data for reactor design or product development.

In order to study the flow fields of RIM machines, boundary conditions can be forced in rotating plates geometry. In RIM, two monomers form a lamellar structure with a scale around 50 μm

in a period of around 100 ms, corresponding to 5 spins of the top plate at a rotational speed of 50 Hz for a gap between plates of 1 mm (Fonte et al. 2011).

Different flow regimes in RIM machines mixing heads are associated to different topologies of the monomers interface, which can be studied in the rotating plates geometry.

On the other hand, in RIM, the monomers often have quite dissimilar viscosities. The rotating plates geometry will be used to assess the striation thickness of monomers with different physical properties under a similar shearing history to the one occurring in RIM.

Reactive polymerizations, as the production of polyurethanes, polyureas and polyamides-6, are carried out in RIM and the reaction kinetics studies can be made in the plate/plate rheometer.

Nowadays, these topics have increased relevance because these studies generate data for reactor design increasing the yield and energy efficiency of the industrial processes enabling fast product development for reactive polymerization.

1.2 Thesis Objectives and Layout

The objectives of this thesis are the description of the flow in a plate/plate and a cone/plate rheometer, the study of the influence of topology in these systems and the analysis of the mixture of two dissimilar fluids.

The layout of this work is as follows.

In Chapter 2 is summarized the studies in this field and the concepts used in this thesis. This Chapter was divided in four sections: Measurements of the degree of mixing (Section 2.1), Mixing in Microfluids (Section 2.2), Mechanistic mixing models − the lamellar model (Section 2.3) and Mixing in hydrodynamics simulation (Section 2.4).

Chapter 3 focuses on a CFD simulation of a plate/plate geometry. Firstly, the physical domain (Section 3.1), the governing equations, the boundary conditions (Section 3.2) and the domain discretization (Section 3.3) are described. Then, the numerical solution at steady state is obtained using Ansys Fluent. In Section 3.4, a mixture of two fluids with glycerol properties, initially side-by-side, is simulated and the degree of mixing is studied using the scale of segregation concept. Afterwards, the topology is changed and the solution is compared with the previous case (Section 3.5). Then the influence of rotation (Section 3.6), the analysis of numerical diffusivity (Section 3.7) and the mixing between two fluids with different properties (Section 3.8), glycerol and water, are addressed.

The experimental tests are described in Chapter 4. In the rheological tests, the device used was a cone/plate system. Firstly, the technique used and the experiments carried out are described in Section 4.1 and, thus, results are presented and discussed in Section 4.2.

In order to understand the results obtained, a cone/plate geometry was simulated in Ansys Fluent as described in Chapter 5. Firstly, the physical domain (Section 5.1), the governing equations (Section 5.2), the boundary conditions (Section 5.2) and the domain discretization (Section 5.3) are summarized and, then, the hydrodynamics is simulated and obtained in Chapter 5.4. Finally, the mixing of two similar fluids, i.e., fluids with the same properties, is studied in Section 5.5 while mixing between dissimilar fluids is addressed in Section 5.6.

2 State of the Art

Mixing is a unit operation that is common in chemical and physical processes where a mixture is produced by distributions of components throughout the volume of the system (Ottino 1980).

Over the last fifty years, the literature published on mixing was scarce. However, in 1952, Danckwerts introduced the concept of Residence Time Distribution (RTD) and two measures for fluid non-homogeneities: Intensity of Segregation and Scale of Segregation (Danckwerts 1952). The evolution of scales in a mixture was thoroughly described from the lamellar model (Ottino, Ranz, and Macosko 1978) and from chaotic system theories that had a significant boost over the 1980s from the work of Prof. Julio Ottino (Ottino 1997).

The development of computational resources has had a major role in the study of mixing mechanisms enabling numerical resolutions of flow and mass transfer equations through model simulations. Computational Fluid Dynamics (CFD) is a numerical tool based on the governing equations of flow and mass transfer that, nowadays, enables accurate numerical experiments of mixing in chemical reactors at transition flow regimes (Santos, Dias, and Lopes 2012).

There are some topics about mixing that have been addressed in literature, as measurements of the degree of mixing, mixing in microfluidics, mechanistic mixing models − the lamellar model and mixing in hydrodynamics simulation. These topics are discussed below.

2.1 Measurements of the Degree of Mixing

One of the problems in the study of mixing was its quantification because there was "no quantitative method of expressing goodness of mixing" (Danckwerts 1952). Spencer and Wiley (1951) introduced the concept of interfacial area between two components and Danckwerts (1952) solved the problem of quantification introducing two concepts: scale of segregation and intensity of segregation.

The scale of segregation is a measure to quantify the degree of homogeneity of the fluid which is defined by

$$S_s = \int_0^\infty R(r)\, dr \tag{1}$$

where $R(r)$ is the mean correlation coefficient between two points of the mixture a distance r apart, and is defined by

$$R(r) = \frac{\overline{(\alpha(x) - \bar{\alpha})(\alpha(x + r) - \bar{\alpha})}}{\overline{(\alpha(x) - \bar{\alpha})^2}} \tag{2}$$

where α is the volume fraction function, and x is the spacial coordinate.

The intensity of segregation is a measure of the deviation from the mean of the concentration of a species in the clumps of fluid, and for a mixture with two species, 1 and 2, is defined by

$$I_s = \frac{\sigma_{C_1}^2}{\bar{C}_1 \bar{C}_2} \tag{3}$$

where ,C_1 is the concentration of the species 1, $\sigma_{C_1}^2$ is the variance.

The scale of segregation can be only affected by mechanical energy supplied while the intensity of segregation depends on diffusion. The mechanisms that can reduce the scale of segregation are shearing, folding and stretching (Mohr, Saxton, and Jepson 1957a).

The degree of homogeneity of the fluids is related to physical methods. In addition to physical methods, the quantification of mixing can be done using chemical methods that use the spectrum of products from a chemical reaction (Santos, Dias, and Lopes 2012). But, in this work, this method is not analyzed.

2.2 Mixing in Microfluidics

The first mixing models were based on the description of the mass transfer from one phase to another rather than on the actual mixing mechanisms. These models are called phenomenological models (Santos, Dias, and Lopes 2012).

Ottino and Wiggins (2004) assessed the phenomenological models of mixing in microfluidics. Microfluidics is a term used to describe flow in devices having dimension ranging from millimeters to micrometers. In the last few years, this area has had an outburst of the number of published works.

Ottino and Wiggins (2004) examined fluid flow in a channel under the following conditions: channel length $l \approx 200\,\mu\text{m}$; velocity $U = 1\,\text{cm/s}$; ratio between viscosity and density of $10^{-5}\,\text{cm}^2/\text{s}$; and molecular diffusion coefficient, D_m, between $10^{-5}\,\text{cm}^2/\text{s}$ and $10^{-7}\,\text{cm}^2/\text{s}$.

To inspect the influence of diffusion on mixing, the authors concluded that the Péclet Number, given by

$$Pe = \frac{Ul}{D_m} \tag{4}$$

ranges from 10^1 to 10^5, i.e., $Pe \gg 1$, thereby, convection is much faster than molecular diffusion. Therefore, even in small reactors at steady and transitional flow regimes, molecular diffusion may be neglected in this mixing process (Ottino and Wiggins 2004).

2.3 Mechanistic Mixing Models — the Lamellar Model

In laminar-flow systems, the main mixing mechanism is shearing and the effect of diffusion is neglected. Figure 3 shows the motion of an element of fluid in a system of two fluids of equal viscosity enclosed between parallel plates where the upper wall is moving. The induced shear stretches out the particle enclosed, creating a striation of the laminas (Mohr, Saxton, and Jepson 1957a).
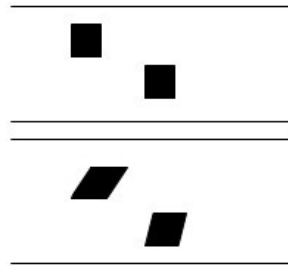
Figure 3 Mixing action of fluid shear

Therefore, the mixing action of fluid is the striation thinning of laminas, constituted by the initial components (Mohr, Saxton, and Jepson 1957a). Modeling based on the deformation of the fluid was an attempt to fill a gap in the knowledge of non-turbulent mixing.

Moreover, in the same year, Mohr investigated mixing in a single-screw extruder where shear rate is the main mixing mechanism. The quantities of shear received by an element of fluid were used to calculate the goodness of mixing, expressed by the striation thickness (Mohr, Saxton, and Jepson 1957b).

The lamellar model was proposed by Ottino, Ranz, and Macosko (1978). This model consists on the deformation of the fluid structures by the mechanism of stretching and folding giving rise to strias.

Ottino, Ranz, and Macosko (1978) began by defining the striation thickness. Figure 4 illustrates the concept of striation thickness and interfacial area for a mixture of two fluids separated by equally spaced parallel surfaces (Ranz 1979).

Figure 4 Striation thickness in ideal lamellar structure

The striation thickness is defined by

$$s = \frac{\delta_A + \delta_B}{2} \tag{5}$$

where δ_A and δ_B are the thicknesses of each component (Ottino, Ranz, and Macosko 1978).

If s is too small, i.e., less than 1 nm or less, a good level of mixing is achieved (Ottino, Ranz, and Macosko 1978).

The average combined width of the laminas of two fluids, in other words, the striation thickness, is a measure of the scale of segregation. For a uniform stripped pattern of a binary mixture, the scale of segregation, S_s, is related to the striation thickness, s, by (Fonte 2012)

$$s = 4\,S_s \qquad (6)$$

Ottino, Ranz, and Macosko (1978) also studied the stretching properties of the flow from a Lagrangian point of view, tracking the translation of an element of fluid in the flow. The element with an initial radius, $|dX|$, is advected. Figure 5 shows the translation of the element (Ranz 1979).
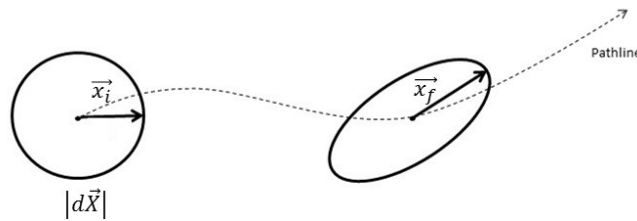
Figure 5 Deformation of an infinitesimal spherical element in time where dx is the displacement

The stretch ratio, λ, can be defined by

$$\lambda = \frac{|d\vec{x}|}{|d\vec{X}|} \qquad (7)$$

where $|d\vec{x}|$ is equal to the deformation, i.e., $|d\vec{x}| = \vec{x_f} - \vec{x_i}$ and $|dX|$ is the radius of each element (Fonte 2012).

If $\lambda > 1$, the system is being stretched while if $0 < \lambda < 1$, it is being compressed (Fonte 2012).

In the lamellar model, the initial length of the fluid is δ_0, and under a shear, at time t, the length is δ_t. So, the stretch ratio is given by

$$\lambda = \frac{\delta_t}{\delta_0} \qquad (8)$$

In pure shear flows and when the components are becoming aligned with streamlines, the stretching is linear ($\lambda \propto t$). A greater interfacial area for transfer and the decrease of striation thickness increases the concentration gradients and thus the mass flux.

The deformation of materials promotes an increase of interfacial area and striation thickness thinning, accelerating the inter-diffusion of components. This originates enhanced diffusion by steeping concentration gradients around the mixture components interface.

Ottino, Ranz, and Macosko (1978) developed an equation for the interfacial area generation and introduced tools to analyze mixing between two fluids with instabilities at microscale and without surface tension effects. Ottino (1980) used the lamellar model to find the concentration field in a system with multicomponent diffusion.

Later, Fields and Ottino (1987) used the lamellar model to predict the effect of striation thickness distribution on polymerization of a polyurethane. Two different distributions were used: a uniform distribution and another that was obtained experimentally from impingement mixing in RIM. In terms of conversion, the best results obtained were with the uniform distribution and it was observed that the distribution of striation thickness has a great impact on the final conversion. Also, the effect of stretching could have a great impact on mixing. Two cases were studied: shear flow and elongation flow. The authors observed that the elongation flow promotes mixing more efficiently (Santos, Dias, and Lopes 2012).

Nowadays, the lamellar model has a field of application on reactive polymerization from liquid monomers, where two streams of high viscosity (100 to 2000 mPa·s) are mixed in a laminar flow field inside an opposed jets reactor, as in RIM, and the original thickness is decreased (Santos, Dias, and Lopes 2012).

2.4 Mixing in Hydrodynamics Simulations

Computational Fluid Dynamic (CFD) is based on principles of mass conservation, momentum conservation (Newton's Second Law) and energy conservation (First Law of Thermodynamics). The set of equations chosen for the flow description considers incompressible fluids and neglects the body forces. The mass conservation equation is expressed by

$$\nabla \cdot v = 0 \tag{9}$$

and the momentum conservation equation is given by

$$\rho \left(\frac{\partial v}{\partial t} + v \cdot \nabla v \right) = -\nabla p + \mu \, \nabla^2 v \tag{10}$$

Equation (10) corresponds to the Navier-Stokes equations.

The energy equation for Newtonian fluids with density (ρ) and viscosity (μ) constants is

$$\rho C_p (\frac{\partial T}{\partial t} + v \cdot \nabla T) = K \nabla^2 T + \mu \phi_v \tag{11}$$

where K is the thermal conductivity of the material and $\mu \phi_v$ is the viscous dissipation of the flow.

The advection-diffusion-reaction equation that describes the mass transfer field is given by

$$\frac{\partial C}{\partial t} + v \cdot \nabla C = D_m \nabla^2 C + R \qquad (12)$$

where v is the velocity, p is the pressure, C is the concentration of a chemical species, D_m is the molecular diffusivity coefficient and R is the net rate of creation of the chemical species by chemical reaction (Santos, Dias, and Lopes 2012).

These equations are based on *ab initio* description of the flow, and so the simulation of mixing between fluids from these equations can be considered as a numerical experiment.

3 3D CFD Modeling of Mixing in a Plate/Plate Geometry

The geometry addressed in this chapter is known in rheometry as the plate/plate rotational geometry and it is similar to rotor/stators mixers. These rotation devices promote well-defined flows enabling to set a very homogeneous distribution of mixing scales throughout the flow domain.

3.1 Physical Domain

A 3D geometrical domain was considered to simulate the flow. The domain consists of two plates with a diameter of 10 mm and spaced by 1 mm, i.e., in cylindrical coordinates, the boundaries of the geometry are, $r = 5$ mm, $z = 0$ mm and $z = 1$ mm (Figure 6).

In this geometry, the upper plate is the moving part and the bottom plate is fixed.
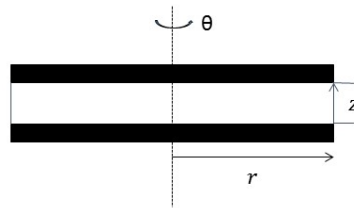
Figure 6 Plate/plate rheometer

3.2 Governing Equations and Boundary Conditions

The set of equations chosen for the flow description considers incompressible fluids and neglects the body forces. The equations used to describe the flow were the mass conservation equation and the momentum conservation equation. The energy conservation equation is not taken into account because isothermal conditions are considered.

The boundary conditions imposed to the simulation are the velocities of the walls, where the bottom of the cylinder is a stopped plate and the top is rotating. The angular speed of the upper plate is 0.01 rad/s. On the other hand, the side walls have no shear stresses condition. In this case, a fluid (glycerol) was enclosed between the two parallel plates.

Glycerol is a Newtonian fluid with a density of $\rho = 1259.9 \text{ kg/m}^3$ and a viscosity $\mu = 0.799 \text{ Pa} \cdot \text{s}$. These values are available in database of Ansys Fluent.

In order to know the flow regime, the Reynolds number was calculated by

$$Re = \frac{\rho \, \omega \, D \, h}{2 \, \mu} \tag{13}$$

where ω is the angular speed (rad/s), D is the diameter of the plate (m) and h is the space between the two plates (m).

The Reynolds number is 7.9×10^{-5} , i.e., $Re << 1$, resulting in creeping flow regime without secondary flow or flow separation.

3.3 Domain Discretization

The mesh distribution is of key importance for a high quality model, in other words, to solve the flow and gradients efficiently. Therefore, the geometry was discretized with 6.6×10^6 elements with a volume of $1.3 \times 10^{-13} \, m^3$ per element. Each element has a hexaedrum geometry with an edge of $0.05 \, mm$. The geometrical domain and the grid for flow simulations were generated with the software packages *DesignModeler* and *Meshing* included in Ansys 16 suite.

As the rotation axis of the two plates is the region where the folding occurs, this area must be more refined. For this reason, the cylinder was built from five bodies refined differently: in the center, the body is more refined while surrounding bodies are less refined (Figure 7)

Grid refinement studies were not carried out because, since the regime is laminar, there is no secondary flow. Furthermore for this flow, there are analytical solutions that enable model validation. However, it could have some interest to make some grid studies with less refined mesh to speed up the simulations time.
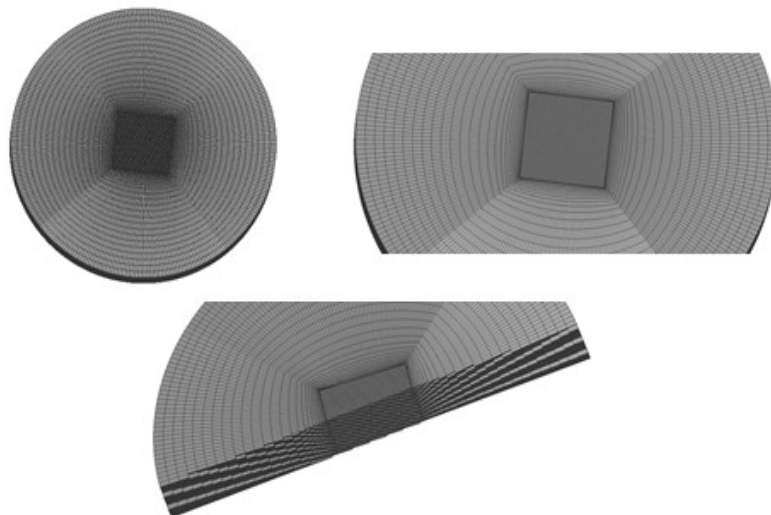
Figure 7 Mesh Distribution

Numerical Solution at Steady State

The flow equations were solved with the finite-volume commercial CFD solver Ansys Fluent 16 using the computational cluster Grid FEUP that has 32 nodes each with 16 cores and 64 GB of RAM.

Initially, the CFD simulations are set for steady state, i.e., the transient terms are zero. Glycerol was set as the working fluid.

In steady state simulations, the SIMPLE scheme was used for the pressure-velocity coupling. Also, Second Order and Second Order Upwind schemes were used for the numerical spatial discretization of pressure and advective terms of Equation (10), respectively. As the objective is the validation of the results, the case was simulated for the following residuals value: 10^{-4}, 10^{-6} and 10^{-7}.

3.3.1   Velocity Profile

The flow between two plates is defined by concentric streamlines parallel to each other because the rotational motion creates a velocity profile along the radius that is zero at the center and maximum at a distance r from the center. The tangential velocity is determined by $v = \omega r$ (Figure 8).
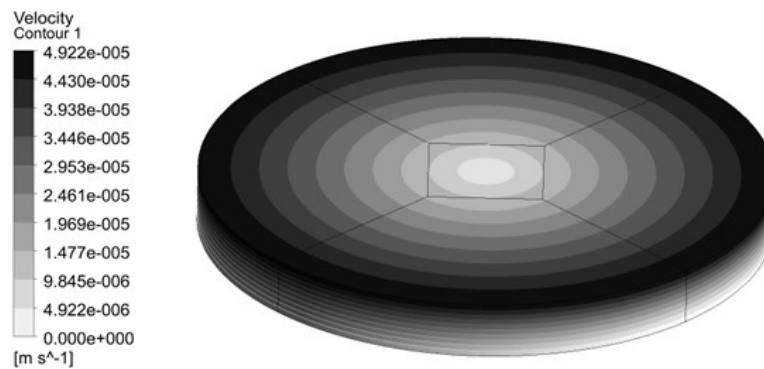
Figure 8 Veloctiy map at the position z=1 mm for a plate/plate rheometer

On the other hand, as the bottom plate is stationary, a velocity profile between the two plates is created (Figure 9). This fact occurs due to the force, $\vec{F}$, applied to the upper plate which makes the upper plate rotate. Thereby, a pure shear flow is generated where adjacent layers of fluid slide over each other with different speeds due to the gradient of the velocity in cylindrical coordinates, $\frac{du}{dz}$, in the normal direction, z.
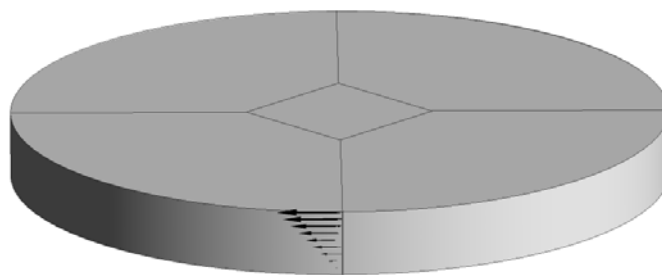
Figure 9 Velocity profile on z-direction at outside wall for a plate/plate rheometer

When the flow conditions are formulated with cylindrical coordinates, the only non-zero component of velocity is in the θ-direction, $v_\theta(r, z)$, i.e., $v_r = 0$, and $v_z = 0$. In order to know the θ-velocity, the equation of motion can be studied through tensor analyses for steady state, $\left(\frac{dv}{dt}\right) = 0$,

$$r: -\frac{\rho v_\theta^2}{r} = -\frac{\partial p}{\partial r} \tag{14}$$

$$\theta: \frac{1}{r^2}\frac{\partial}{\partial r}(r^2 \zeta_{r\theta}) + \frac{\partial \zeta_{z\theta}}{\partial z} - \frac{\zeta_{r\theta}}{r} = 0 \tag{15}$$

$$z: \frac{\partial p}{\partial z} + \rho g = 0 \tag{16}$$

where $\zeta_{r\theta}$ is the tensor in the θ-direction to the r-direction and $\zeta_{z\theta}$ is the tensor in the θ-direction to the z-direction. As the geometry is too small, gravitational forces can be neglected.

As referred above, glycerol is a Newtonian fluid and the tension exerted can be given by Newton's law of viscosity, $\zeta_{r\theta} = -\mu \frac{\partial v_\theta}{\partial r}$. The equation of motion for a Newtonian fluid in the θ-direction is given by

$$\mu\left[\frac{\partial}{\partial r}\left(\frac{1}{r}\frac{\partial}{\partial r}(r\, v_\theta)\right) + \frac{\partial^2 v_\theta}{\partial z^2}\right] = 0 \tag{17}$$

The solution of Equation (17) is a linear profile along the r and z-directions

$$v_\theta = \frac{r\,\omega\,z}{h} \tag{18}$$

where h is the height of the cylinder defined by the plate/plate geometry (Macosko 1993).

In order to compare the velocity profile described by Equation (18) with the solution obtained in Ansys Fluent, Figure 10 shows both velocity profiles at the outside wall for the three residuals values set as the convergence criterion.

(a)   (b)
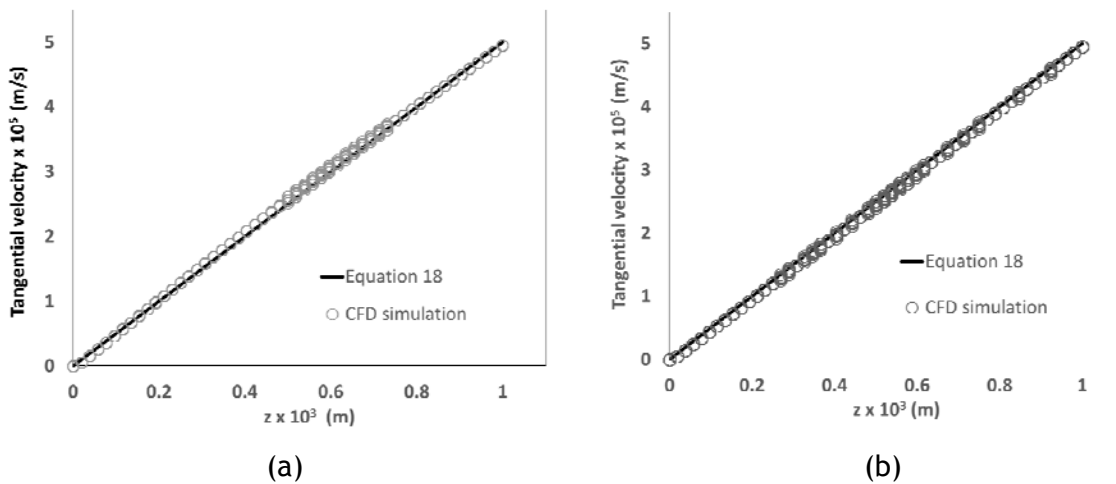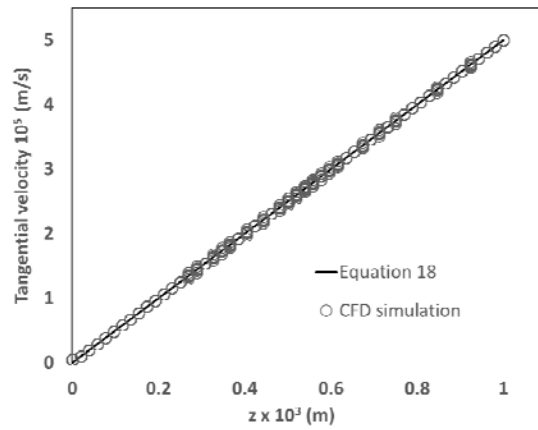
(c)

Figure 10 Comparison between analytical solution of the flow and simulation results at the outside wall for (a) Residuals 10^{-4}; (b) Residuals 10^{-6}; (c) Residuals 10^{-7}

The analytical solution of the flow from Equation (18) is well described by the CFD simulation results (Figure 10), showing that the velocity profile at the outside wall is linear in the z-direction. Other curves in the z-direction at different distances from the plate center, perpendicular to the top plate, were plotted and, as Figure 11 shows, the profiles are linear over the entire flow.
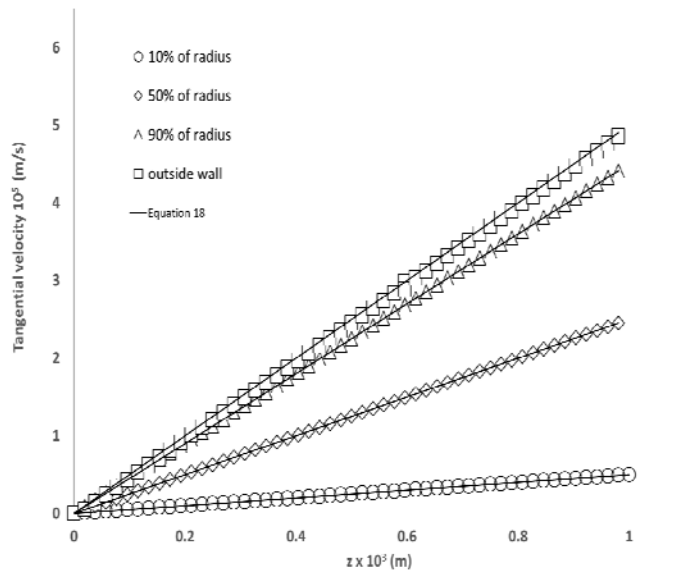
Figure 11 Velocity profiles in z-direction at different positions of the center for plate/plate rheometer (Residuals of 10^{-7})

However, Macosko (1993) suggested that Equation 18 is only valid for a geometry where the space between the two parallel disks is small. Therefore, the gap between the plates was changed to 4 mm. From Figure 12, it is possible to conclude that the velocity profile in the z-direction is not linear and a height of 4 mm is enough for Equation (18) to lose the validity.
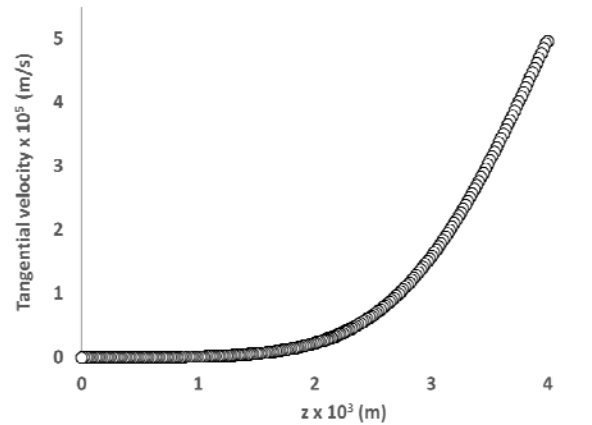
Figure 12 Velocity profile in z-direction for system with plates spaced by 4 mm

3.3.2 Pressure Profile

The pressure profiles were also obtained in study the influence of pressure drop on the velocity field and Figure 13 shows the respective pressure contour map. The variation in pressure in the θ-direction is expected to be zero otherwise there would have been discontinuities. Although Figure 13 seems to indicate that there are some variations in pressure along the θ-direction, the velocity profile agrees with the expected profile (Equation (18)) and, consequently, the solution was accepted.
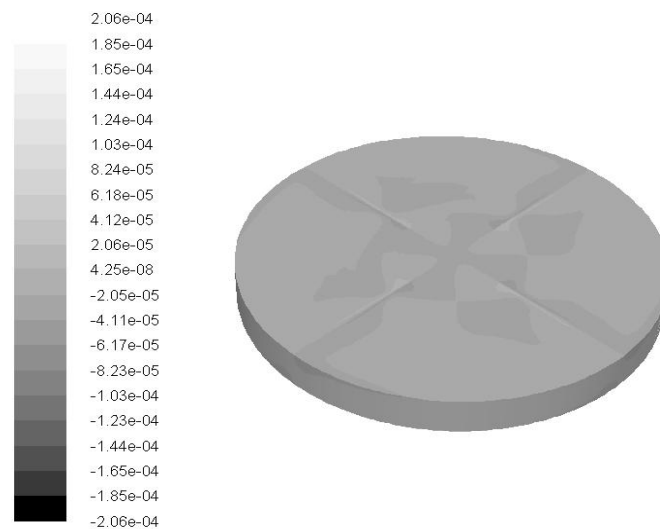
Figure 13 Pressure map for the plate/plate geometry in Pa

3.4 Mixing of Fluids with the Same Properties

Ansys Fluent includes three Euler-Euler multiphase models: Volume-Of-Fluid (VOF) model, mixture model and Eulerian model. Since at this scale, the main mixing mechanism is not diffusion, but shearing, the VOF model was used to simulate the dynamics of mixing of two phases in the flow.

In the VOF model, mass transfer is given by

$$\frac{\partial \alpha_{glycerol}}{\partial t} + \nabla \cdot \left(\alpha_{glycerol} \, v \right) = 0 \qquad (19)$$

where $\alpha_{glycerol}$ is the volume fraction of glycerol. When $\alpha_{glycerol} = 0$, it means that there is no glycerol and when $\alpha_{glycerol} = 1$, it means that there is only glycerol. It should be noted that this model differs from Equation (12) because diffusion is neglected.

The volume fraction of phase A, α_A, is determined by (Ansys 2016)

$$\sum_i \alpha_i = 1, i = \{glycerol, A\} \qquad (20)$$

Low order numerical schemes for the discretization of advective term of Equation (19) can produce artificial mixing of two fluids induced by numerical diffusion. This numerical problem can be solved with a higher resolution discretization scheme, an interface reconstruction method or a high grid refinement near the interface. Simulations using this model track the interface between two phases, i.e., the interface is reconstructed. Also, in this model, the value of the diffusion coefficient between the two phases and the surface tension at the interface are zero (Fonte 2012).

The SIMPLE scheme was used for the pressure-velocity coupling and PRESTO! and First Order Upwind were used for pressure and momentum. On the other hand, the First Order Implicit scheme was used for the discretization of the transient terms of Equations (19) and (10) and Geometric Reconstruct Scheme was used in reconstruction of the interface position. The Geometric Reconstruct Scheme assumes that the interface between two fluids has a linear slope within each cell and uses this linear shape for calculation of the advection of fluid (Ansys 2016).

For the dynamic simulations, a value of 10^{-4} for residuals of all variables was used as the convergence criterion since, as observed in Figure 10, this value is adequate to obtain velocity profiles as described by Equation (18).

The dynamic simulations were started from the steady state solution of the flow fields after setting the VOF model and dividing the cylinder in two phases. The phases were composed of two fluids with glycerol's properties, i.e., two similar fluids. The initial topology is illustrated in Figure 14.
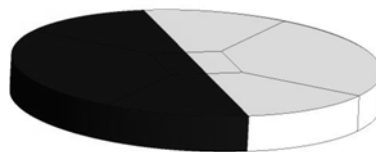
Figure 14 Topology 1

The time step chosen was defined as

$$\Delta t = \frac{\Delta x \, C_N}{\omega \, r} \tag{21}$$

corresponding to a Courant number, C_N, equal to 1, where Δx is the edge length of an element, ω is the angular speed and r is the radius of the plate. Two time steps were chosen: 0.1 and 0.05 s. The considered number of time steps enabled the plate to rotate, at least, two turns.

3.4.1 Results and discussion

Figure 15 shows the results of rotation of the top plate at four different times: initial time (0 s), half turn ($\approx$ 314 s), one turn ($\approx$ 628 s) and two turns ($\approx$ 1256 s). For different integration step, the results obtained are similar because position of each fluid is equal.

(a) (b)

(c) (d)
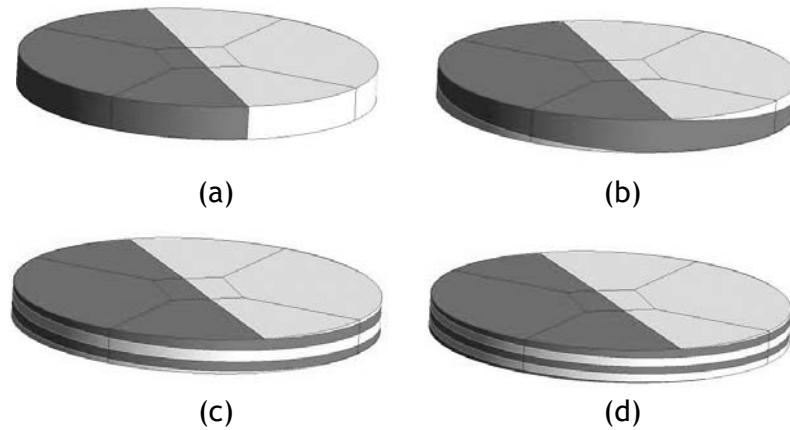
Figure 15 Plate/plate geometry in different states of rotation (a) initial time (b) half rotation (c) one rotation (d) two rotations

In rotational devices, mixing occurs due to stretching of the interface between two phases, in other words, each element of interfacial area is stretching along time. Initially, the interfacial area length is $\delta_0 = h$ and after a turn ($\approx$ 628 s), $\delta_t = 2\pi r$, i.e., the length is stretched to the perimeter of the plate. The stretch ratio is given by Equation (8) and is linear in time

$$\lambda = n \, \frac{2\pi r}{h} = \frac{t}{628} \, \frac{2\pi r}{h} \tag{22}$$

where n is the number of rotations, r is the radius of the plate (m), h is the height between the two plates (m) and t is the time (s).

As expected, the motion of the top plate induces shear and creates a lamellar structure with two strias. Each stria is composed of a white and a black strip. Figure 16 shows the chart of volume fraction of glycerol vs z after two turns and the corresponding map.

<center>(a)   (b)</center>
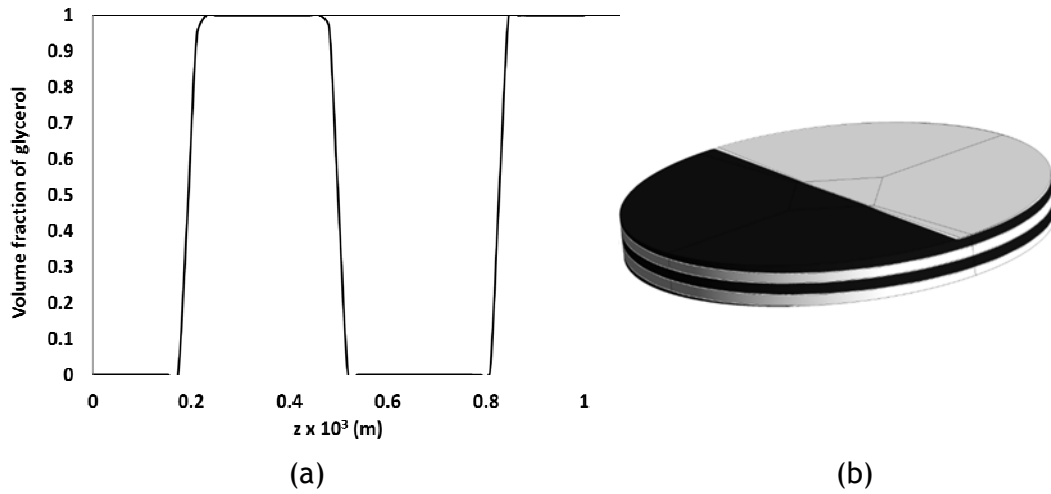
Figure 16 Volume fraction profile after two turns and the corresponding map

After two turns, two strias were formed. So, h is divided in 4 lamellae. The concentration profile is defined by

$$\alpha(z) = \left[H(z) - H\left(z - \frac{h}{4}\right)\right] + \left[H\left(z - \frac{h}{2}\right) - H(z - \frac{3h}{4})\right] \tag{23}$$

The scale of segregation for the profile defined by Equation (23) was calculated from Equations (1) and (2), using Matlab. Using the mean correlation coefficient, the integral of Equation (2) is

$$S_s = \frac{h}{8} \tag{24}$$

However, since the strip is uniform, the striation thickness is equal to one quarter of scale of segregation (Equation (6))

$$s = \frac{h}{4} \tag{25}$$

In order to know the variation of scale of segregation with the number of turns, the number of lamellae after rotating three and five times was analyzed.

Figure 17 shows the concentration profiles after the upper plate rotates five and eight times. From these profiles, it could be concluded that there is a linear relationship between the number of spins and the number of strias. Using the method described previously, the scale of segregation for each rotation position was calculated.

(a)   (b)
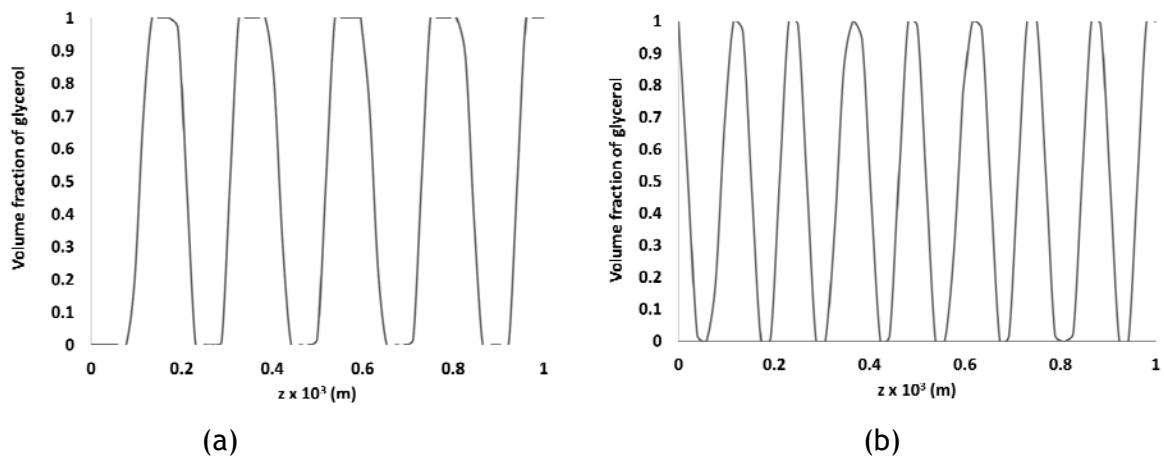
Figure 17 Concentration profile (a) after the upper plate rotates five times (b) after the upper plate rotates eight times

The reduction of mixing scale and generation of interfacial area in this device are entirely set by the number of turns,

$$s = \frac{h}{2n} \tag{26}$$

where n is the number of spins.

3.5 Influence of Topology

When the flow has predominant direction for shearing, as the case of a plate/plate rotational rheometer, the initial position of the reactants, i.e., the topology, plays a major role on the evolution of mixing scales.
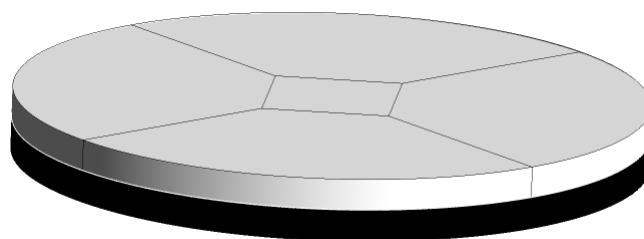
Figure 18 Topology 2

In order to know the influence of the topology for mixing degree, the two phases were set over each other parallel to the top rotating plate (Figure 18). The model is the one used in the Section 3.4. As the case above, the fluids have the glycerol's properties.

3.5.1   Results and Discussion

Figure 19 shows the phase maps after the top rotates a half turn and one turn.

<center>(a)   (b)</center>

Figure 19 Two different states of rotation (a) half rotation (b) one rotation

The rotating plate creates a force that, consequently, creates a gradient of velocity $\left(\frac{du}{dz}\right)$. The interfacial area between phases is parallel to the velocity field (Figure 9 and Figure 19). Then, the interface is rotating and there is no stretching of the interface as in the case of Topology 1. Similarly to the rotating plate, the interface between phases has a smaller velocity in the center than at the periphery (Figure 8).

In conclusion, the mixing scales and interfaces of both phases are kept without any change due to the topology of the two phase interface.

3.6 Influence of Rotation of Upper Plate

To investigate the influence of the rotation of the top plate, simulations were performed where the direction is changed alternately at the end of each cycle. During the first turn, the top plate is rotating clockwise and, in the second one, it is spinning counter clockwise and so on. The expression that translates the direction of rotation is

$$\omega = 0.01 \sin\left(\frac{\pi}{628}\, t\right) \tag{27}$$

The rotation of the top plate was imposed as a boundary condition in Ansys Fluent through the definition of a User Defined Function (UDF).

The case was simulated in transient state using the VOF model. The methods used were the SIMPLE scheme for the pressure-velocity coupling, PRESTO! for pressure, Second Order Upwind for momentum, the First Order Implicit scheme for the discretization of the transient terms of Equations (19) and (10) and Geometric Reconstruct Scheme for the reconstruction of the interface position.

The simulation started from the converged case for a residual value of 10^{-4}, in steady state.

3.6.1 Results and Discussion

Figure 20 shows the system after one-quarter, half, three-quarter and one wavelengths. After one turn, the space between the two plates is divided by two striations, however after an anti-rotation the system returns to its initial state.

(a) (b)

(c) (d)
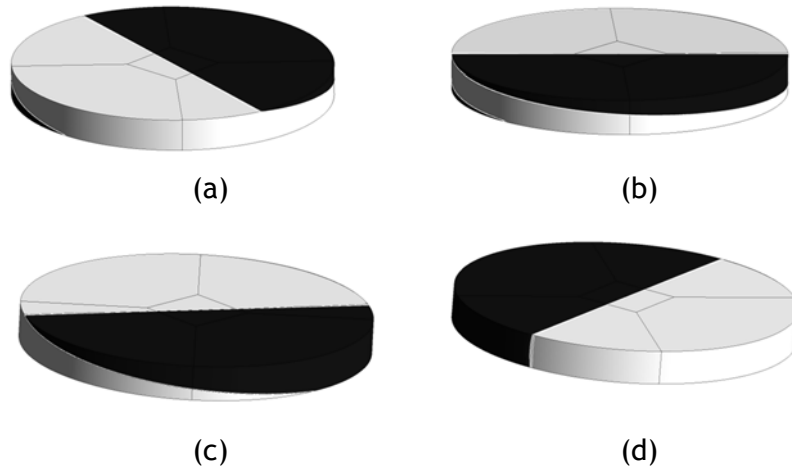
Figure 20 Phase maps after (a) half turn; (b) one turn; (c) half anti-rotation; (d) one anti-rotation

The reasons for the system to return to its original state when the flow changes the direction are: the system is reversible, the fluid is incompressible, the flow is isothermal and there is no diffusion.

3.7 Influence of Numerical Diffuvisity

Molecular diffusion is a mass transfer mechanism where molecules move from a region of high concentration to a region of low concentration. Therefore, the molecular motion attenuates concentration gradient.

Nevertheless, in computer simulations, diffusion can be greater than molecular diffusivity due to numerical diffusion. Low order numerical schemes for discretization of advective term of the Navier-Stokes equation can produce numerical diffusivity (Fonte 2012). Consequently, the simulated system behaves differently than the physical system.

For diffusivity calculations, the species transport equation is used enabling to set parameters related to the calculation of mixing of two fluids. The species transport equation models the mixing and the transport of chemical species by solving the conservation equation describing convection, diffusion and reaction sources for each species. The conservation equation is given by

$$\rho \frac{\partial \alpha_A}{\partial t} + \nabla.(\rho \vec{v} \alpha_A) = -\rho D_m \nabla \alpha_A + R_A + S_A \tag{28}$$

where ρ is the density in kg/m^3, α_A is the mass fraction of chemical species A, $\vec{v}$ is the vector velocity, D_m is the molecular diffusivity in m^2/s, R_A is the net rate of production of species A and S_A is the rate of creation by addition from the dispersed phase plus any user-defined sources. As, in the simulated cases, there is no reaction, the terms R_A and S_A are zero.

Starting from steady state, the methods chosen were the SIMPLE scheme for the pressure velocity coupling, Second Order Upwind for pressure and momentum, the First Order Implicit scheme for the discretization of the transient terms of the momentum Navier-Stokes equations and Second Order Upwind is used for the discretization of mass equation.

For the dynamic simulations, a value of 10^{-4} for residual values of all variables was used as the convergence criterion.

Two fluids with glycerol's properties were set as the working fluids. Initially, the two species were side-by-side as in Figure 14.

To inspect the influence of numerical diffusivity in the simulations, the case studies presented in Table 1 were studied, having each case different initial conditions, for example, different molecular diffusivities, different time steps and concentrations.

Table 1 Case studies of mass diffusivity

Case	Molecular diffusivity ($\mathbf{m^2/s}$)	Time step ($\mathbf{s}$)	Concentration between Glycerol and Glycerol[*]
1	1×10^{-8}	0.1	1/1
2	1×10^{-10}	0.1	1/1
3	1×10^{-10}	0.05	1/1
4	1×10^{-10}	0.05	1/0.01

Glycerol[*] is a substance with same properties (viscosity and density) than pure glycerol.

In order to describe the motion of two species relative to each other, the mass conservation for glycerol is defined from Equation (12) in relation to an inertial frame. The diffusion between the two phases takes place under r, θ and z-directions,

$$\frac{\partial \alpha_{glycerol}}{\partial t} + \frac{v_\theta}{r} \frac{\partial \alpha_{glycerol}}{\partial \theta} = D_{ef} \left[\frac{1}{r} \frac{\partial}{\partial r} \left(r \frac{\partial \alpha_{glycerol}}{\partial r} \right) + \frac{1}{r^2} \frac{\partial^2 \alpha_{glycerol}}{\partial \theta^2} + \frac{\partial^2 \alpha_{glycerol}}{\partial z^2} \right] \quad (29)$$

where D_{ef} is the diffusivity coefficient and is defined as

$$D_{ef} = D_m + D_n \quad (30)$$

where D_m is the molecular diffusivity coefficient and D_n is the numerical diffusivity coefficient.

3.7.1 Results and Discussion

For each case, a concentration profile is plotted from a perpendicular plane to the interface in the top plate after the top plate has rotated a half turn. Figure 21 corresponds to the profiles obtained for each case.
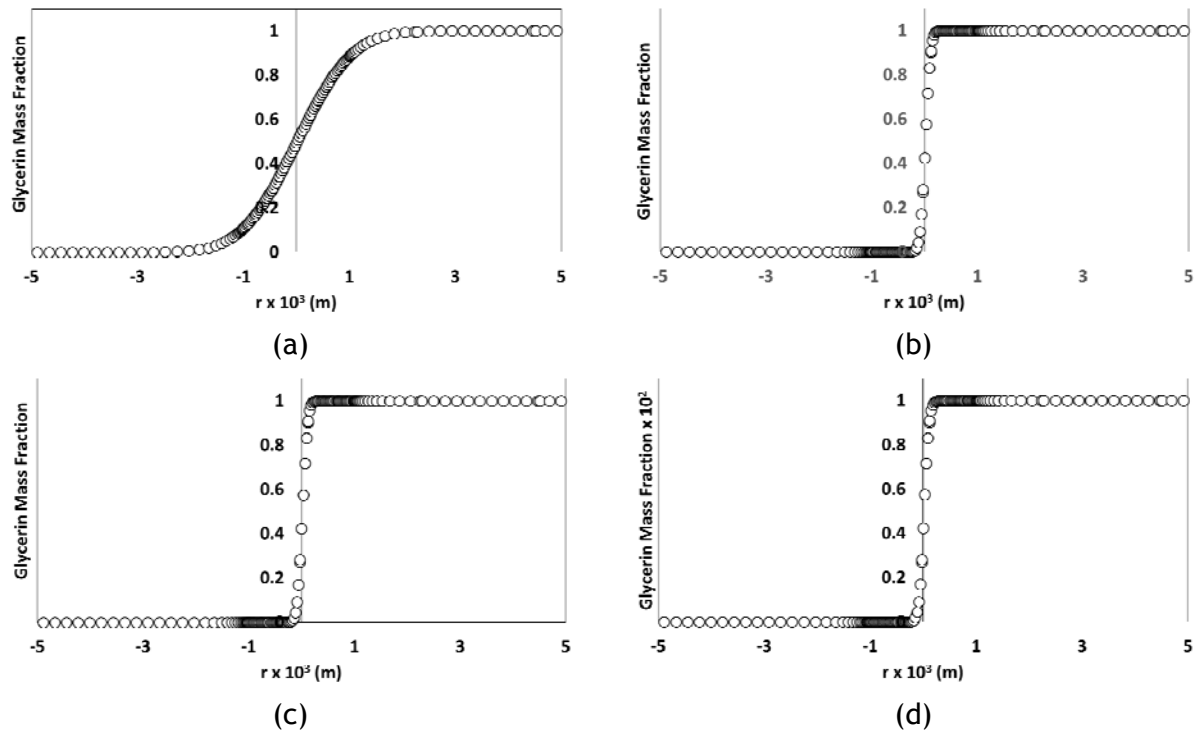
Figure 21 Concentration profile in a plane perpendicular to the interface (a) Case 1; (b) Case 2; (c) Case 3; (d) Case 4

The objective of this section was the computation of D_n to know its influence in the simulations. Thereby, using the Equation 30, D_n is given by the difference between D_m and D_{ef}. D_m is a known value because it is set in Ansys Fluent while D_{ef} can only be determined by the analytical solution of Equation 29 and thus no conclusions were obtained.

3.8 Mixing of Fluids with Different Properties

Physical properties, such as density and viscosity, can influence the mixing degree. In order to study mixing of different fluids, glycerol and water were set as the working fluids. Water has a density of 998.2 kg/m^2 and a viscosity of 0.001 Pa·s according to the database of Ansys Fluent.

The VOF model was used in simulations, hence diffusion will not affect the results.

The methods used were the SIMPLE scheme for the pressure velocity coupling, PRESTO! for pressure, First Order Upwind for momentum, the First Order Implicit scheme for the discretization of the transient terms of the momentum of Navier-Stokes equations and Geometric Reconstruct Scheme for the reconstruction of the interface position.

The simulations in transient state were started from a converged case in steady state for a residual value of 10^{-4}.

At time equal to zero, glycerol and water are side-by-side (Figure 14).

3.8.1   Results and Discussion

The position of each fluid was studied after a half turn. Figure 22 shows the mass fraction map while Figure 23 shows the contour map of glycerol and water at a plane at half height position, parallel to the top plate.
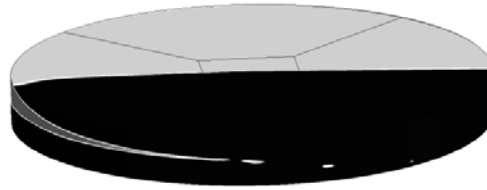
Figure 22 Distribution maps after a half turn (glycerol – black, water – white)
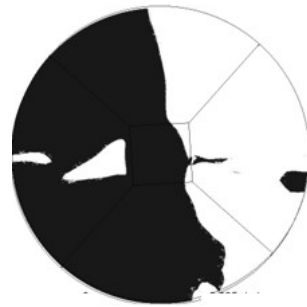
Figure 23 Contour map after a half turn (glycerol – black, water-white) ate the half height plane

Figure 22 shows that the water penetrates the glycerol and Figure 23 indicates that the interface between the two phases is unstable being possible the formation of the fingering patterns. These two phenomena can be related since along of the number of rotations the less viscous fluid is in motion and penetrates the more viscous creating *fingers* of one phase into the other. This phenomenon is called viscous fingering.

Figure 23 also shows that the glycerol is encroaching the center of the system dragging the water to the periphery. This phenomenon occurs due to the conservation of angular momentum. When there is no external force to be exerted, the torque is zero and, consequently, there is conversation of angular momentum.

The angular momentum, $\vec{L}$, can be calculated by the product of the mass, m, and the linear momentum, $\vec{M}$

$$\vec{L} = m\,\vec{M} \tag{31}$$

The linear momentum is given by the product between mass and the tangential velocity,

$$L = m \, \omega \, r^2 \tag{32}$$

Since there is conservation of angular momentum in this system, the ratio between the position of glycerol and water is equal to

$$\frac{r_{glycerol}}{r_{water}} = \frac{\rho_{water} \, \mu_{glycerol}}{\rho_{glycerol} \, \mu_{water}} \tag{33}$$

As a result of Equation (33), $r_{glycerol}$ is bigger than r_{water}. Thereby, the glycerol moves occupying more space in the plate center dragging the water to the periphery.

In order to demonstrate what property (density or viscosity) plays a major role on the motion of glycerol, two cases were simulated. In the first case, the compounds have the same viscosity (glycerol viscosity) and different density. In the other case, they have the same density and different viscosity. Figure 24 shows a plane at a position of half height after one and half turns.
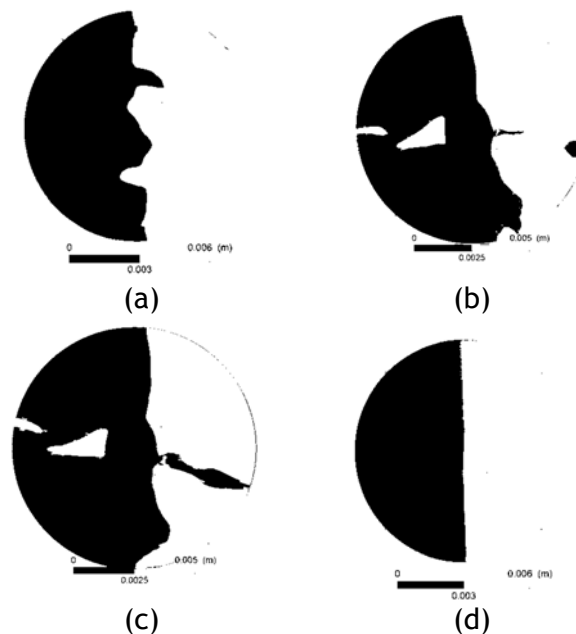
Figure 24 Distribution of mass fraction (glycerol – black and water – white) a) different density, equal viscosity; b) different density and viscosity; c) different viscosity, equal density; d) equal density and viscosity

It is possible to conclude that in Figure 24 (a) and (d), there is no motion of glycerol being the two species in the center of the system, while Figure 24 (b) and (c), the glycerol moves to the periphery occupying more space in the center.

Mathematically, in the case where the density is equal in both phases (Figure 24 (c)), $r_{glycerol}$ is bigger than r_{water}. However, in the case where the viscosity is equal in both phases, the ratio between the two radii is approximately 0.79 being the change in position of each species not visible in relation to the previous case (Figure 24 (a)).

As conclusion, the viscosity is the property which plays the major role in the fact of the glycerol is encroaching the center of the plate/plate system and water is moving to periphery.

4 Experimental Data

As refereed and proved in Chapter 3, the rotational devices used in rheometry presents a well-defined flows enabling to study the evolution of mixing scales for different initial topology. Rheometry is a technique to measure the rheological properties of fluids, such as, viscosity and elasticity.

4.1 Description of Rheometer and Experiments

In this work, the model of the rheometer used was Anton Paar Physica UDS 200 - Universal Dynamic Spectrometer (Figure 25). The system consists of four devices: the rheometer measuring drive, rheometer electronics, thermostatic bath and computer with the control program. The technical specifications of rheometer are summarized in Table 2.

Figure 25 Model of the rheometer used

Table 2 Technical specifications of the rheometer

Torque range	$0.5\ \mu\text{Nm} - 150\ \text{mNm}$
Torque resolution	$0.1\ \mu\text{Nm}$
Angular resolution	$< 1\ \mu\text{rad}$
Frequency range	$10^{-4} - 100\ \text{Hz}$
Shear stress range	$10^{-3} - 10^5\ \text{Pa}$
Shear rate range	$10^{-6} - 10^5\ \text{Hz}$
Viscosity range	$0.5 \times 10^{-3} - 8.5 \times 10^8\ \text{Pa.s}$

In all experiments, the measuring system used was a cone/plate more specifically an MK24 device (Figure 26). In this geometry, the cone is the moving part and the plate is stationary. In the Table 3, the dimensions of this device are described.

Table 3 Dimensions of MK24	
Radius (mm)	37.5
Angle between plate and cone (°)	1
Volume of Sample (mL)	2.2

Figure 26 Cone/plate system

In order to control the temperature, a thermostating bath was connected to the measuring system. TEK 180 is the thermostating bath that operates with a fluid which is circulated through a chamber in the plate and controls the temperature. The operation temperature was 20 ℃.

This rheometer performs rotation and oscillation tests. The rotation tests control shear rate and shear stress while the oscillation tests check strain amplitude and stress amplitude.

In this work, rotation tests were carried out to measure the evolution of rheology of a mixture of two fluids. These methods include flow curve tests and time test measurement. The flow curve tests are performed to obtain flow properties being conducted in shear rate control mode defining a linear or a logarithmic scale shear rate ramp. The time test rotation is used at a constant shear rate and a constant temperature in order to research ageing and reaction changes in the sample (Torres 2014).

The quantities measured by the rheometer are torque, displacement and normal force. These measurements are used to calculate stress, strain, shear rate, viscosity and normal stress.

Glycerol aqueous solutions were set as the working fluids. In the beginning, glycerol was laid on the plate and the cone was lowered to a specified gap height (Table 2). Then, the shear rate, $\dot{\gamma}$, the duration of each measurement and the number of points were specified in the rheometer software: 50 Hz, 50 s and 50 points, respectively.

During the tests, the torque, ζ, is measured and, then, shear stress, τ, is computed from

$$\tau = \frac{3\,\zeta}{2\,\pi\,r^3} \tag{34}$$

where r is the radius of the plate (Macosko 1993).

Then, the viscosity, μ, is reported by the software being estimated through

$$\mu = \frac{\tau}{\dot{\gamma}} \tag{35}$$

At 20ºC, the measured viscosity of glycerol was 1.25 Pa·s. This value can be compared with the experimental correlation (Santos 2003),

$$\mu = \left[\left[(1 - X_{glycerol})(A_{water}e^{\frac{B_{water}}{T}}) \right]^a + \left[X_{glycerol}(A_{glycerol}e^{\frac{B_{glycerol}}{T}}) \right]^a \right]^{1/a} \tag{36}$$

where μ is the viscosity in mPa·s, T is the temperature in K, $X_{glycerol}$ is the amount of glycerol in the samples and the constants are equal to: $A_{water} = 5.14 \times 10^{-6}$ mPa·s, $B_{water} = 2.22 \times 10^3$ K, $A_{glycerol} = 7.06 \times 10^{-9}$ mPa·s, $B_{glycerol} = 7.64 \times 10^3$ K and $a = -0.320$.

The viscosity of glycerol calculated by Equation (36) is 1.45 Pa·s. This difference of viscosities is due to the fact that glycerol absorbs water from the atmosphere being the experimental viscosity smaller than it obtained by Equation (36).

Therefore, glycerol and water were loaded in the rheometer plate according to two different topologies, described in Figures 14 and 18.

To know the influence of diffusion in experiments using Topology 1, the Péclet Number, i.e., the ratio between convection and diffusion, was calculated from Equation (4). Molecular diffusion coefficients, D_m, of glycerol, in a system of glycerol and water, is 1.4×10^{-9} m²/s (D'Errico et al. 2004).

As refereed in Section 2.3, the increase of interface along of the number of rotations accelerates the inter-diffusion of components. Thereby, the mass transfer is given by the rate of the formation of the interface,

$$\dot{a} = \frac{\pi r^2}{t} \tag{37}$$

where r is the radius of plate MK24 ($r = 37.5$ mm) and t is the period of one rotation for a shear rate of 50 Hz ($t \approx 7.2$ s). In this case, Péclet Number is given by the ratio between the rate of the formation of the interface and the molecular diffusion coefficient.

Therefore, the Péclet Number is approximately 5×10^3 indicating that convection is much faster than molecular diffusion.

4.2   Results and Discussion

The experimental results are shown in Figure 27. Four types of tests were carried out:

- mixing of water and glycerol using Topology 1;
- mixing of water and glycerol using Topology 2;

- viscosity measurement of a solution of 50% of water and 50% of glycerol.
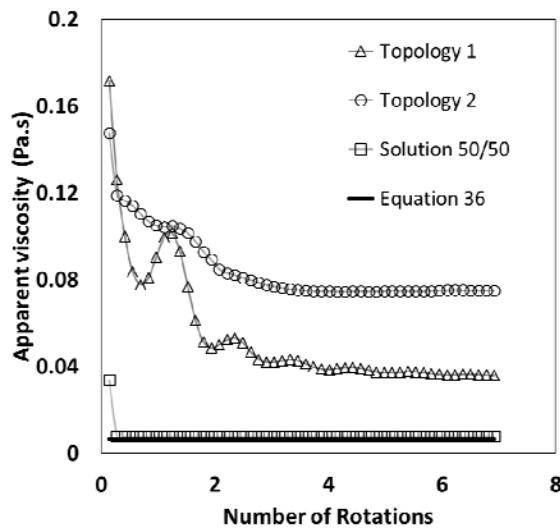
Figure 27 Apparent viscosity versus number of rotations for different topologies for a viscosity ratio 1000

From Figure 27, some conclusions can be drawn about the variation of viscosity. The apparent viscosity in Topology 1 and Topology 2 is greater than in a solution with 50% of water and 50% of glycerol, and this value is consistent with Equation (36). On the other hand, as expected, in Topology 2, the apparent viscosity is constant during the rotation of the upper plate. However, in Topology 1, this property oscillates along of the number of rotations.

In order to interpret the experimental results, the rheological tests were repeated for a viscosity ratio of 10. Thereby, from Equation (36), the $X_{glycerol}$ is calculated to know the amount of glycerol needed to make a solution 10 times less viscous. Figure 28 illustrates the experimental results of the mixing of glycerol and the solution using Topology 1 and the viscosity of a solution of 50% of glycerol and 50% of the solution 10 times less viscous.
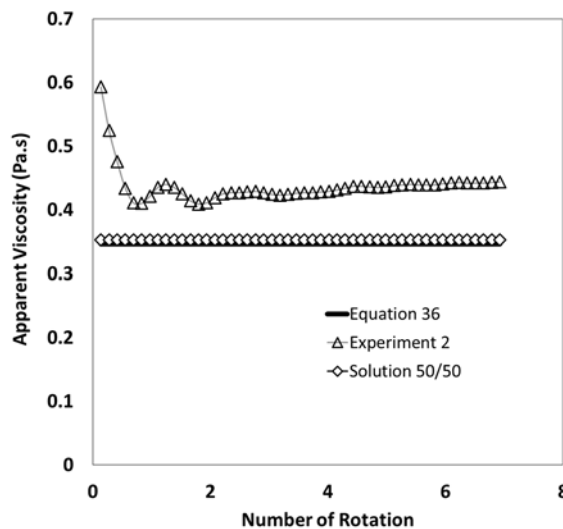

Figure 28 Apparent viscosity versus the number of rotations for Topology 1 for a viscosity ratio of 10

Such as in Figure 27, in Figure 28 the apparent viscosity oscillates along of the number of rotations trending towards a larger value than the viscosity of the 50%/50% solution. The only apparent reason for this is the fact of the position of each fluid changes along of the number of rotations. Therefore, the apparent viscosity was calculated for different rotations states to prove that this is the source for this oscillations.

First, the location of each lamella was drawn in Figure 29 from the analysis of the simulation of mixing in a plate/plate geometry between two fluids with viscosity ratio 1 described in Section 3.4. However, in this case, the black strip corresponds to the glycerol and white strip to the solution 10 times less viscous.
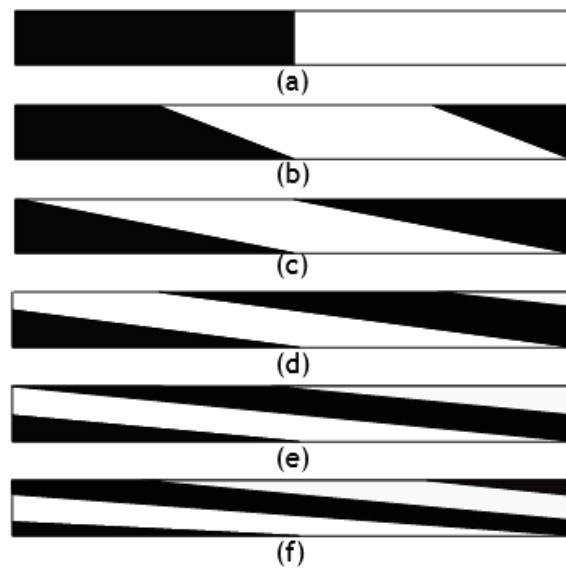
Figure 29 Lamellae position in outside wall (a) in inicial instante; (b) after one quarter of turn; (c) after half turn; (d) after three quarter of turn; (e) one turn; (f) one turn and one quarter

Then, the calculation of the apparent viscosity at each angular position of the upper plate is summarized as follows:

1. Set the time of the rotation and determine the angular position of the upper plate;
2. Set the spatial distribution of the two fluids through the observation of images such as Figure 29. For example, after one quarter of a turn, 25% of the volume is only occupied by glycerol, 25% by the solution and the other 50% is a region with two lamellae. In this lamellae, the position of the glycerol and the solution can be different. In some cases, the glycerol is above the solution and in the others, the position is inverse.
3. Determine the length in each region;
4. Discretization of the length;
5. Definition of the position of the interface for each point of the discretization;
6. Calculation of the velocity of the interface between the two fluids at each point using the equations in Appendix 1and computation of the velocity profiles;

7. Computation of the shear stress in each point from the relative position of the fluids. For example, in a stria with 2 lamellae, when the solution is above the glycerol,

$$\tau_{gly/sol}{}^* = \mu_{glycerol}\,\frac{v^*}{x^*} + \mu_{solution}\,\frac{v_{tang} - v^*}{h - x^*} \tag{38}$$

where $\tau_{gly/sol}{}^*$ is the shear stress in glycerol for each point in a system with 2 lamellae where the solution is above the glycerol, v^* is the velocity of the interface (m/s), x^* is the height of the interface (m) which ranges from 0 to 0.655 mm, h is the height and v_{tang} is the tangential velocity for the outside wall which is calculated using the equation $v = \omega\,r$.

The angular speed is given by,

$$\omega = \dot{\gamma}\beta \tag{39}$$

where β is the angle between the cone and plate and $\dot{\gamma}$ is the shear rate (Macosko 1993). The angular speed of the simulations is 0.87 rad/s. Therefore, the tangential velocity at outside wall, i.e., $r = 37.5$ mm, is 0.03 m/s.

On the other hand, when the position of each lamella is inverse, i.e., when the glycerol is above the solution, the shear stress is given by

$$\tau_{sol/gly}{}^* = \mu_{solution}\,\frac{v^*}{x^*} + \mu_{glycerol}\,\frac{v_{tang} - v^*}{h - x^*} \tag{40}$$

where $\tau_{sol/gly}{}^*$ is the shear stress in the solution for each point in a system with 2 lamellae where the glycerol is above the solution.

8. Integration of the shear stress to know this value in each region

$$\tau_{gly/sol} = \frac{\int_0^L \tau_{gly/sol}{}^*\,dx}{L}\ or\ \tau_{sol/gly} = \frac{\int_0^L \tau_{sol/gly}{}^*\,dx}{L} \tag{41}$$

9. Calculation of the shear rate in the entire domain,

$$\tau = \sum_{j=1}^{\infty} \alpha_j \tau_{gly/sol,j} + \alpha_j \tau_{sol/gly,j} + \alpha_{j-1} \tau_{gly/sol,j-1} + \alpha_{j-1} \tau_{sol/gly,j-1} \tag{42}$$

where j is the number of lamellae and α is the volume fraction.

10. Estimation of the apparent viscosity of the system for defined time

$$\mu_{app} = \frac{\tau\,\Delta h}{\Delta v} \tag{43}$$

where Δh is the gap between two plates, i.e., 0.655 mm, and Δv is the difference of velocities between the cone and plate. As the plate is stopped, i.e., $v = 0$, and the velocity of cone is 0.03 m/s, the difference of velocities is 0.03 m/s.

For the beginning the rotation, the two fluids are side-by-side, i.e., 50% of the volume of the system is composed of glycerol and the other part of a solution 10 times less viscous. So, the apparent viscosity (μ_{app}) is calculated by

$$\mu_{app} = 0.5 \times \mu_{glycerol} + 0.5 \times \mu_{solution} \qquad (44)$$

where $\mu_{glycerol}$ is the glycerol viscosity, i.e., 1.22 Pa·s and $\mu_{solution}$ is the viscosity of the solution 10 times less viscous, i.e., 0.122 Pa·s. So, the apparent viscosity is 0.671 Pa·s.

In Figure 30, the values calculated and the experimental curve are plotted in order to compare them.
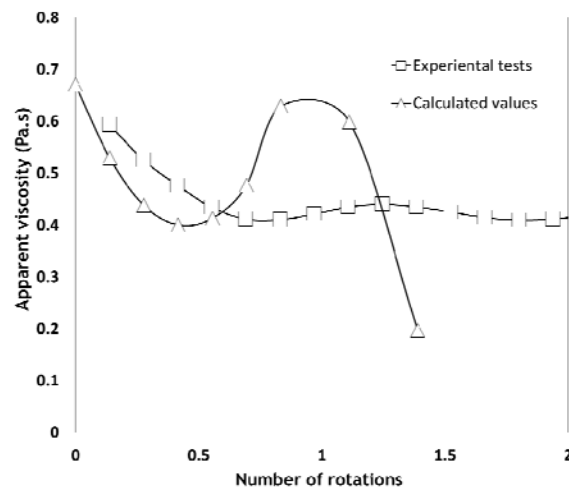

Figure 30 Comparison between the apparent viscosity calculated and the obtain in the experimental tests

Figure 30 shows that both the calculated values and the viscosity measured in rheometer are not constants along of the number of rotations, however, the curves are not similar. Initially, the apparent viscosity decreases and after half rotation, it starts to increase, but the values detected by the rheometer present a slight delay. Then, the calculated values increase to 0.68 Pa·s while the experimental viscosity has a maximum increase at 0.48 Pa·s. Later, the viscosity decreases again but, here, the values present a great difference and significant delay between them.

Although the curves are not similar, the source of the oscillation of the apparent viscosity could be the formation of the lamellae over the time. The differences between the experimental and calculated values could be a wrong consideration of the position of each lamella since the measurements in the rheometer were carried out with a viscosity ratio of 10 and the lamellae position in the model are taken from Figure 29 for a viscosity ratio of 1. On other hand, as the fluids have different properties, the presence of viscous fingering can contribute for the difference between the results. In this way, this case should be simulated to have more concrete conclusions.

5 3D CFD Modeling of Mixing in a Cone/Plate Geometry

Aiming a deeper insight into the source of the oscillation of the apparent viscosity curve with the number of cone rotations in the rheological tests, a cone/plate rheometer is simulated for the tests conditions of the tests in Chapter 4.

5.1 Physical Domain

A 3D geometrical domain is used to simulate the flow in a cone/plate system. The domain incorporates a cone with an angle of 1° and a plate. The plate has a radius of 37.5 mm. According to Figure 31, r ranges from 0 to 37.5 mm, θ from 0 to 0.017 rad and φ ranges from 0 to 2π rad.

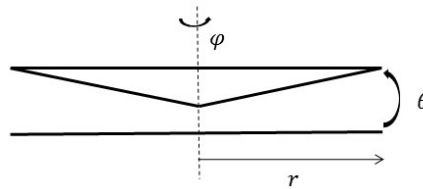In this geometry the cone is the moving part and the plate is fixed.

Figure 31 Cone/plate geometry

5.2 Governing Equations and Boundary Conditions

The boundary conditions imposed to the simulation are the velocity of walls, where the cone is the moving part and plate is stationary. In rheological tests, the operation shear rate, $\dot{\gamma}$, is 50 Hz and is related to angular speed, ω, through Equation (39). Thereby, the angular speed of the simulations is 0.87 rad/s. The outside and inside walls have no shear conditions.

The steady state was simulated with glycerol. In the Ansys Fluent database, glycerol properties correspond to a mixture of glycerol and water. Thus, the properties are estimated by experimental curves and set in Ansys Fluent. The viscosity is given by Equation (36) and density is determined by

$$\rho = \left(1 - X_{glycerol}\right) \rho_{water} + X_{glycerol} \ \rho_{glycerol} \tag{45}$$

where ρ_{water} and $\rho_{glycerol}$ are the densities of water and glycerol, respectively. A solution of 100% of glycerol presents a density of 1261.77 kg/m^3 and a viscosity of 1.45 Pa·s.

In the cone/plate rheometer, the Reynolds number is given by (Bataineh 2014)

$$Re = \frac{\rho\, w\, \beta^2\, r^2}{\mu} \qquad\qquad (46)$$

The Reynolds number is 3.24×10^{-4} , i.e., Re << 1, corresponding to creeping flow regime without secondary flow or flow separation.

5.3 Domain Discretization

The geometry was discretized with 9.9×10^5 elements with a volume of $1.9 \times 10^{-12}\ \text{m}^3$ per element. Each element has a cubical geometry with an edge of $0.125\ \text{mm}$. The geometrical domain and the grid for flow simulations were generated with the software packages *DesignModeler* and *Meshing* included in Ansys 17 suite.

The cone is truncated at a height of $50\ \mu\text{m}$ from the plate and defines an angle β =1° with the plate. In the truncated region, the cone is in contact with the plate and, in this way, there is no flow in this region. In order to have a homogeneous mesh, the domain is divided in different concentric annulus, each one with 2.86 mm of radius (Figure 32).
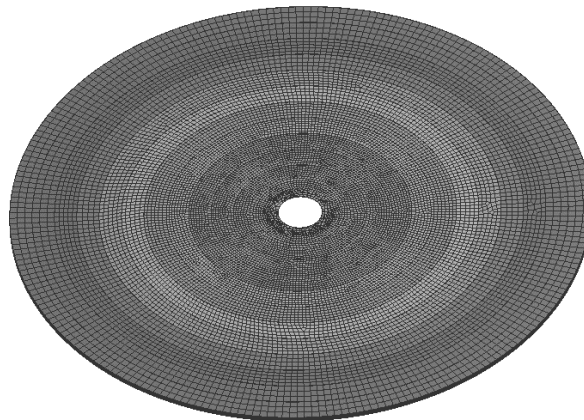
Figure 32 Mesh distribution in system cone/plate

5.4 Numerical Solution at Steady State

The flow equations were solved with the finite-volume commercial CFD solver Ansys Fluent 17 using a PC that has 8 cores with 24 GB of RAM.

In steady state simulations, the SIMPLEC scheme was used for the pressure-velocity coupling. Also, Second Order and Third Order MUSCL schemes were used for the numerical spatial discretization of pressure and momentum terms of Equation (10), respectively. The results were accepted when the simulations are converged, in steady state. As the objective is to validate the results, the case was simulated for the following residual values: 10^{-3}, 10^{-4}, 10^{-6} and 10^{-7}. After the solution is converged to 10^{-3}, the residuals are decreased for 10^{-4} but the case did not converge to this value. Then, the case was simulated in transient time with a large time step,

i.e., 1 s. When the residual value is reached, the steady state was switched on to conclude if the case converges. For the other residuals, the same procedure was carried out.

5.4.1 Velocity profile

The flow created between the plate and the cone due to the rotational motion of the cone, defines a velocity profile along the radius (Figure 33). The tangential velocity is zero in the center and maximum at the periphery, $v = \omega r$.
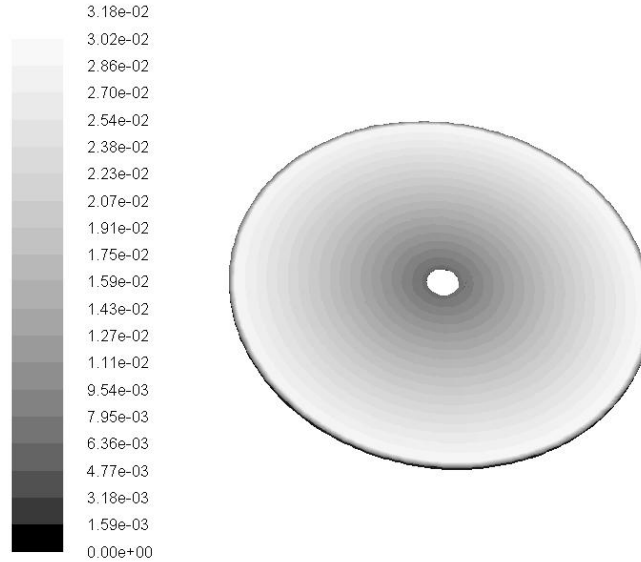

Figure 33 Velocity map in cone - plate/cone system in m/s

On the other hand, a velocity profile between plate and cone is generated due to the difference of the velocity between the wall below and the wall above. When the flow conditions are formulated with spherical coordinates, the only component of velocity is the φ-direction, $v_\varphi(r, \theta)$, with $v_r = 0$ and $v_\theta = 0$.

Such as the glycerol is a Newtonian fluid, the motion for steady state is given by

$$r: -\frac{\rho v_\varphi{}^2}{r} = -\frac{\partial p}{\partial r} \tag{47}$$

$$\theta: -\frac{\rho v_\varphi{}^2 \cot\theta}{r} = -\frac{1}{r}\frac{\partial p}{\partial \theta} \tag{48}$$

$$\varphi: 2r\frac{\partial v_\varphi}{\partial r} + r^2\frac{\partial^2 v_\varphi}{\partial r^2} + \frac{\partial^2 v_\varphi}{\partial \theta^2} + \cot\theta\frac{\partial v_\varphi}{\partial \theta} - \operatorname{cossec}\theta^2 v_\varphi = 0 \tag{49}$$

As the geometry is small, gravitational forces can be neglected.

Macosko (1993) presents an equation that is a good approximation of the solution of the Equations 47, 48 and 49,

$$v_\varphi = \frac{w\,r\,\theta}{\beta} \tag{50}$$

In Cartesian coordinates, Equation (50) can be written as

$$v = \frac{w\,r}{\beta} \arctan\left(\frac{z}{r}\right) \tag{51}$$

To compare Equation (51) and the solution obtained in Ansys Fluent, both velocity profiles were plotted at the outside wall (Figure 34). Figure 34 (a) corresponds to the case simulated for a residual value of 10^{-3}. For this value, the curve is not linear. Decreasing the residuals to 10^{-4}, 10^{-6} and 10^{-7}, the curve converges to the velocity profile described by the equation proposed by Macosko (1993).
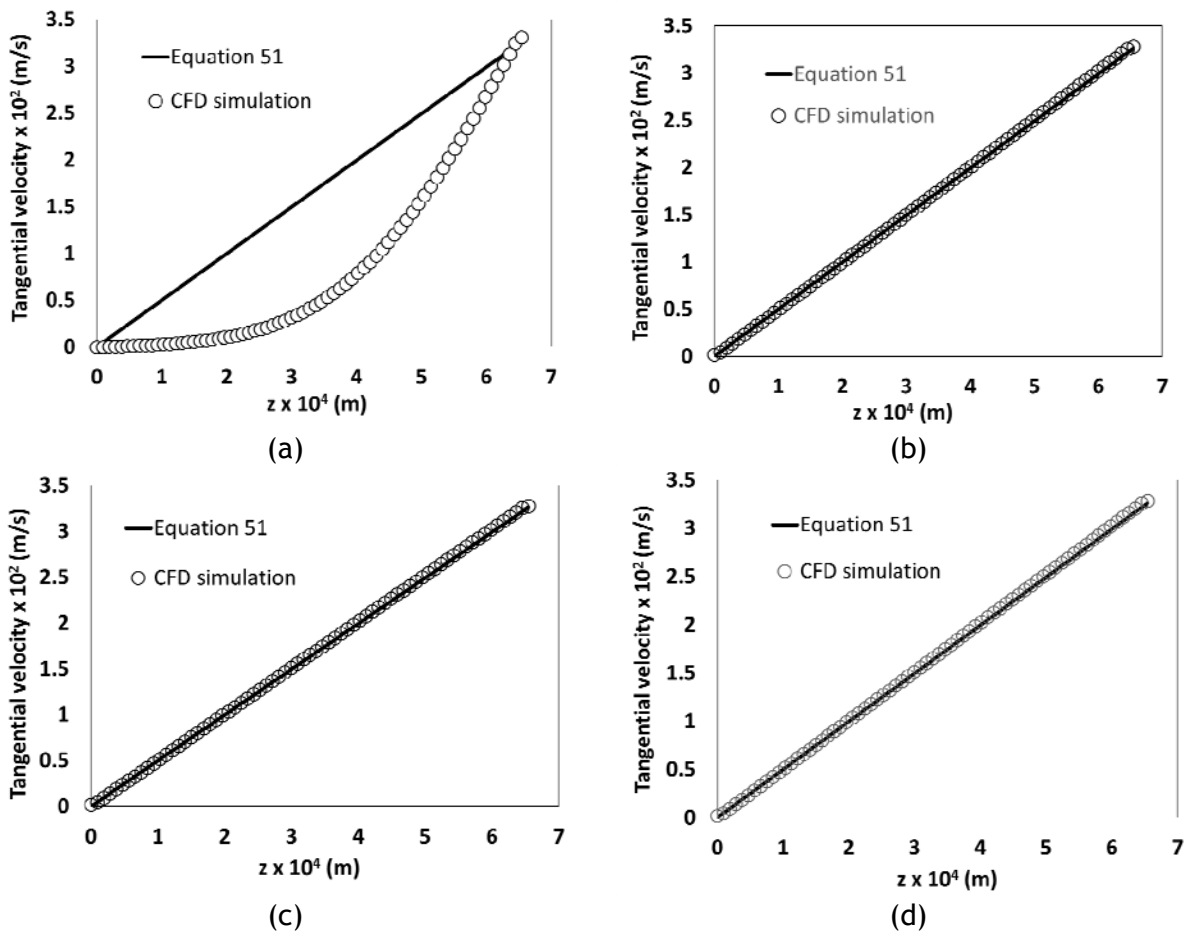

Figure 34 Tangential velocity profile along z-direction at outside wall (a) Residuals 10^{-3}; (b) Residuals 10^{-4}; (c) Residuals 10^{-6}; (d) Residuals 10^{-7}

Other curves in the z-direction at different distances from the rotation axis were plotted to compare with Equation (51). The lines at a distance of 10%, 50% and 90% of radius are represented in Figure 35.

(a)

(b)

(c)
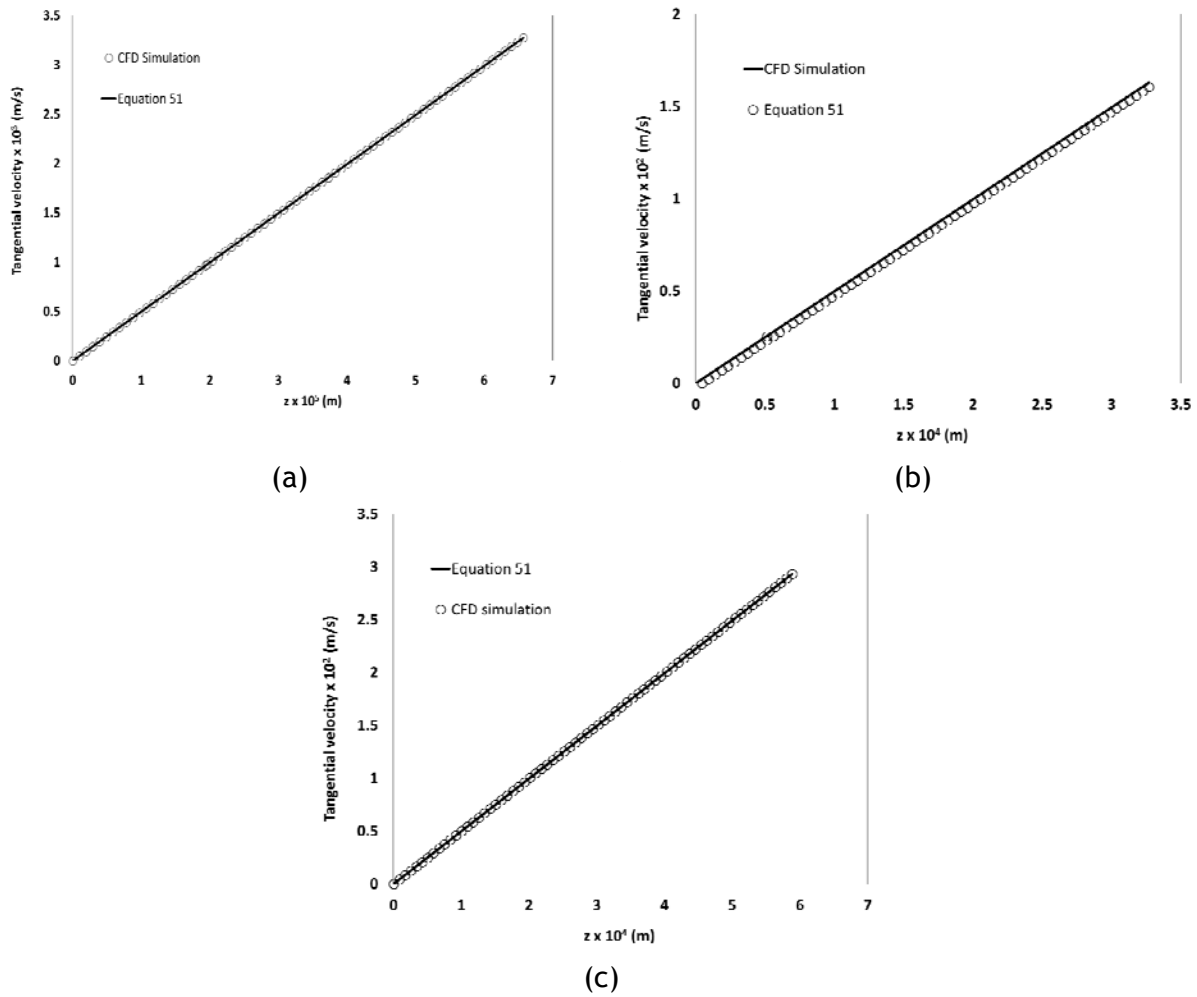
Figure 35 Velocity profiles at different positions from the rotation axis (a) 3.75 mm; (b) 18.75 mm; (c) 33.75 mm

To inspect the validity of the boundary conditions used, the velocity profile at the inside wall was plotted for the simulated case where the residuals are 10^{-7}. Figure 36 (a) shows clearly that the curve is not linear unlike the equation proposed by Macosko (1993). Therefore, the residuals were decreased to 10^{-8} to understand if the curve could tend to the linearity. However, the curve still does not present a linear relation between the tangential velocity and the *z*-direction.

(a)

(b)

Figure 36 Velocity profile in inside wall (a) Residuals 10^{-7}; (b) Residuals 10^{-8}

The pressure profile should be studied to inspect its influence of on the velocity profile.

5.4.2 Pressure Profile

As the profile at the inside wall is not expressed by Equation (51), the study of pressure profile should be made to verify the quality of the solution obtained (Figure 37).

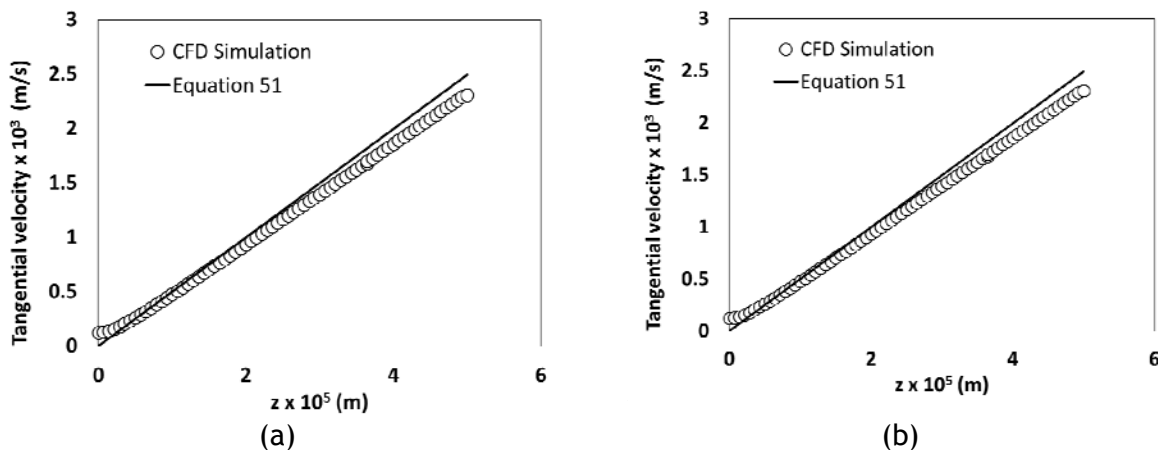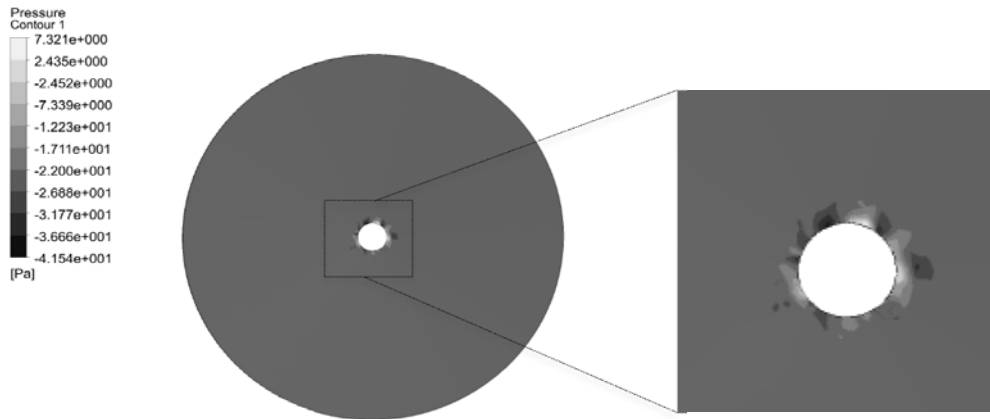*Figure 37 Pressure map – cone/plate system*

From Figure 37, a pressure variation is observed at the center of the domain. This phenomenon can be the answer for the nonlinearity of velocity profile at inside wall. However this fact should be neglected because these pressure drop variations do not affect the velocity profile in the entire system. Nevertheless, it can be monotorised during the next simulations.

5.5 Mixing of Fluids with the Same Properties

As in the plate/plate geometry, the mixing of similar fluids was simulated. Both fluids have the glycerol's properties corresponding to a viscosity ratio of 1 and placed side by side as shown in Figure 38.

Figure 38 Topology 1 - two fluids are side-by-side

The species transport equation was the model set for mass transfer since the VOF model considers two immiscible fluids being the interface between them reconstructed along of time.

As the major objective is to reproduce the experiments, the model chosen must consider that the two fluids are miscible.

The SIMPLEC scheme was used for the pressure-velocity coupling, the Second Order for pressure and the Third Order MUSCL for momentum. On the other hand, the First Order Implicit 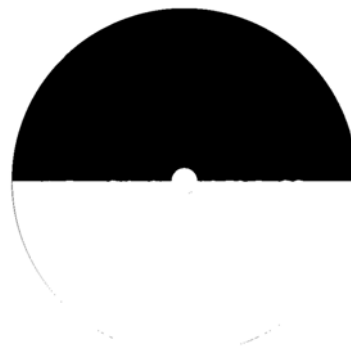scheme was selected for the discretization of the transient terms of Equations (19) and (10). For the mass transfer of the equation, the Second Order Upwind was the method used.

For the dynamic simulations, the flow equations were switched off and the simulation started from the convergence to a residual value of 10^{-8}. The residual value of mass term was 10^{-12} s.

The mass equations were solved with the finite-volume commercial CFD solver Ansys Fluent 17 using computational cluster Grid FEUP that has 32 nodes each with 16 cores and 64 GB of RAM.

Defining the time step from Equation (21), the value achieved was, approximately, 10^{-3} s.

5.5.1   Results and Discussion

Figure 39 illustrates the results of rotation of the cone at three different times: half rotation (≈ 3.6 s), one rotation (≈ 7.2 s) and two rotations (≈ 14.4 s).

(a)

(b)

(c)
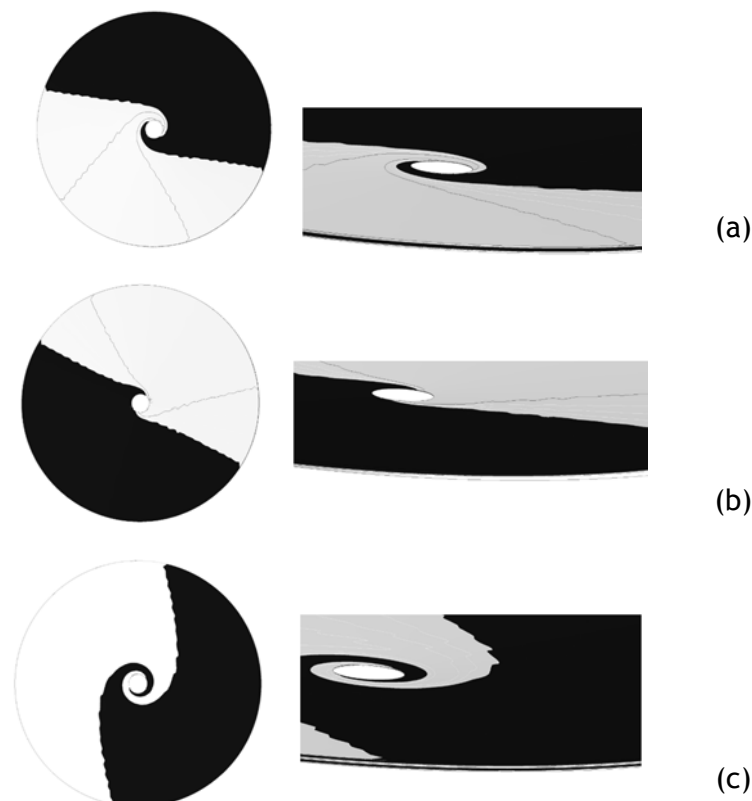
Figure 39 Cone/plate rheometer in different states of rotation for a time step of 10^{-3} (a) half turn; (b) one turn; (c) two turns

As it is possible to see in Figure 39, at the interface, the velocity is not the same at all points and, in this way, the flow is delayed in the inside wall creating the illusion that the interface slides over the time. Decreasing the time step for 10^{-4} s, Figure 40 shows this phenomenon remains quite considerable.

(a)

(b)

(c)

(d)

Figure 40 Cone/plate rheometer in different states of rotation for a time step of 10^{-4} (a) one quarter of rotation; (b) half turn; (c) one turn; (d) two turns

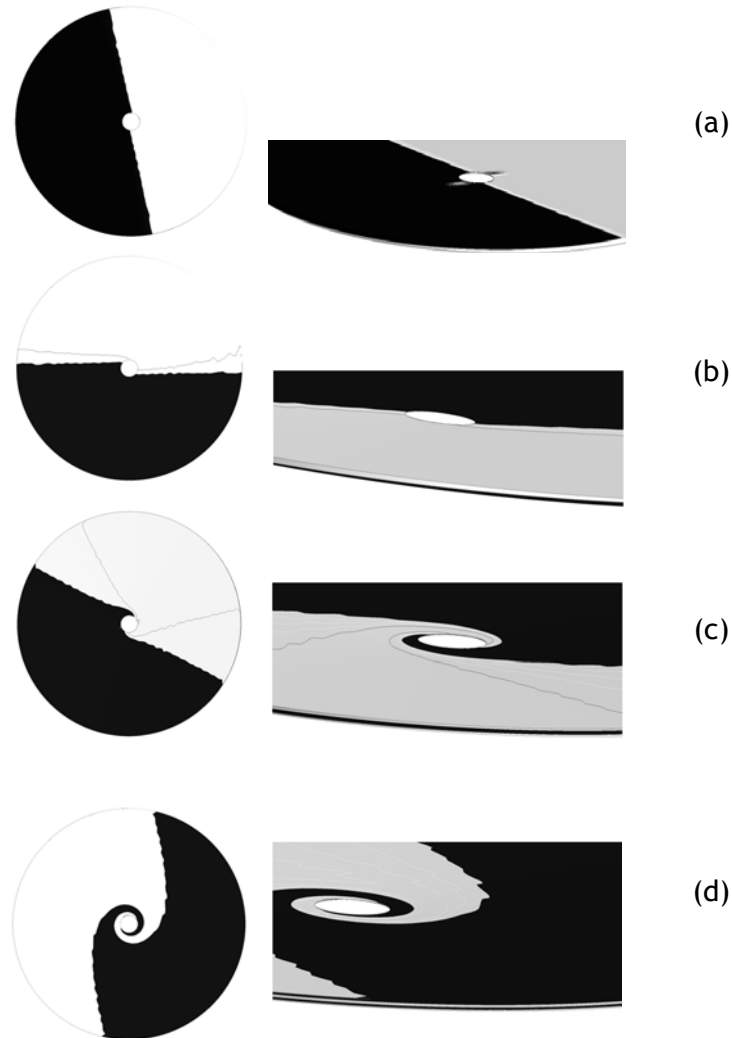Decreasing again the residual values to 10^{-5} s, Figure 41 shows the mass fraction distribution after one quarter of rotation.

Figure 41 Cone/plate rheometer in different states of rotation for a time step of 10^{-3} one quarter of rotation

Comparing Figure 40 (a) and Figure 41, it is possible to conclude that the slip of the fluid in inside wall can be smaller when the residual value decreases. However, the time of the simulation is too short to draw conclusion.

After two turns, two lamellae were formed. Therefore, the gap between the cone and the plate is divided in 4 lamellae being the concentration profile defined as

$$\alpha(z) = \left[H(z) - H\left(z - \frac{\beta R_p}{4} \right) \right] + \left[H\left(z - \frac{\beta R_p}{2} \right) - H\left(z - \frac{3\beta R_p}{4} \right) \right] \tag{52}$$

Using the same method used in Section 3.4.1., for a flow in cone/plate rheometer the striation thickness is given by

$$s = \frac{\beta R_p}{2n} \tag{53}$$

where n is the number of turns, R_p is the radius of the plate and β is the angle between the cone and the plate in rad.

Althought there is some numerical divergence regarding the tracking of the fluids interface at the walls, the flow is well validated from Equation (51) as can be seen in Figure 42 (a).

(a)   (b)
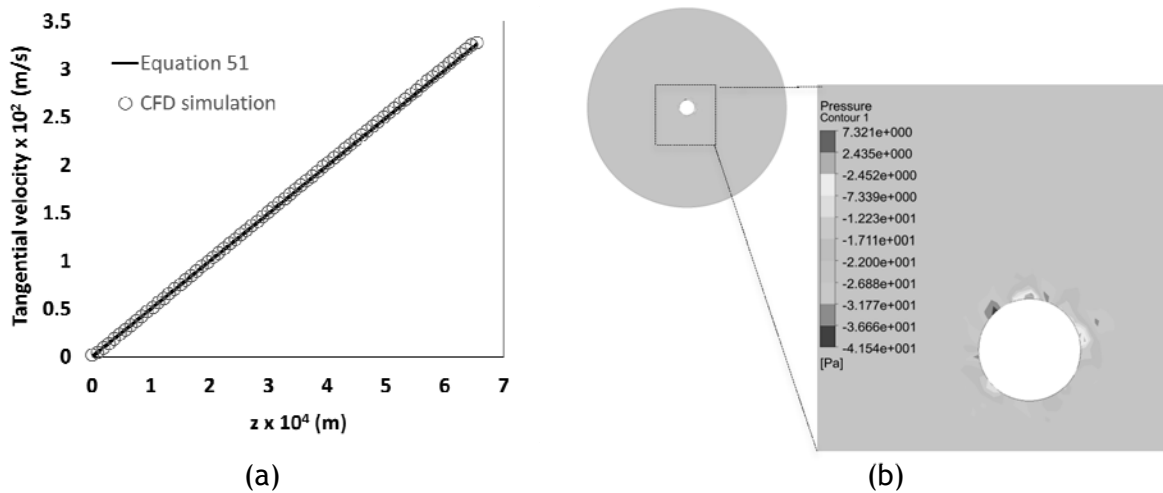
Figure 42 Velocity (a) and pressure map (b) in Pa for ratio 1

Figure 42 (b) further shows that at the center of the domain a variation of pressure is observed, as was the at in steady state. This solution was considered valid because the velocity profile is given by Equation (51).

5.6 Mixing of Fluids with Different Properties

Appling the same topology of the case above, the viscosity ratio between two fluids was set to 2 and 10 in order to reproduce the experimental tests of Chapter 4.

Glycerol and species A were the fluids used. In Table 4 are summarized the properties of the species A.

Table 4 Properties of the species used in experiments with dissimilar fluids

	μ_A (Pa • s)	ρ (kg/m^3)
Ratio 2	0.73	1254.4
Ratio 10	0.15	1230.3

The model used was the species model and the methods for the calculations were the same used in previously case.

For the dynamic simulations, the simulation started from the convergence to a residual value of 10^{-8}. The residuals of mass term was 10^{-12}.

5.6.1   Results and Discussion

Starting from the results of viscosity ratio 2, Figure 43 illustrates the results of the rotational motion of the plate after 0.03 s. Since the simulation time is too short, the flow delay of the interface in the inside wall is not verified such as in the ratio 1 (Section 5.5). However with a higher simulation time, this phenomena can be observed.
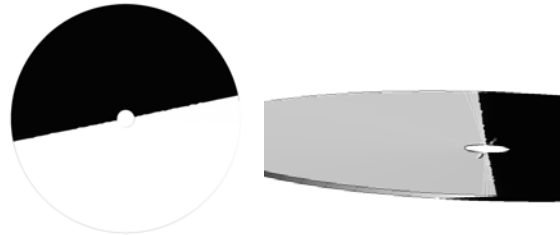

Figure 43 Result of the distribution of each fluid after 0.03 s

In the rheological tests, it was found that the viscosity oscillates over time. Hence, the shear stress was registered from Ansys Fluent and the viscosity was calculated from Equation (35) and shown in Figure 44.
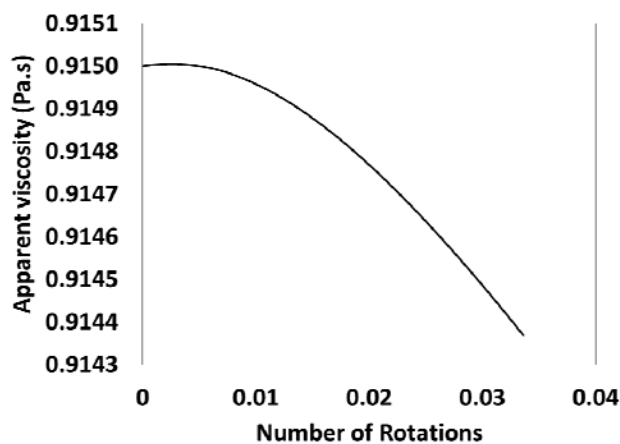

Figure 44 Shear stress in the top Wall versus the number of rotations for ratio 2

As expected, initially, the apparent viscosity is equal to 50% of glycerol viscosity and 50% of the viscosity of the solution 2 times less viscous. In this way, the viscosity should be 0.915 Pa·s corresponding to the initial value refereed in Figure 44. As the rheological tests reported, in the first half rotation, the viscosity should decrease followed by an increase. Since the simulation took too long, the time obtained is short being impossible to see this change in the behavior.

Figure 45 corresponds to pressure and velocity profiles for the mixing of two fluids with viscosity ratio 2. As the case above, the velocity profile is given by equation proposed by Macosko (1993). On the other side, the pressure is different depending on the position of fluids.
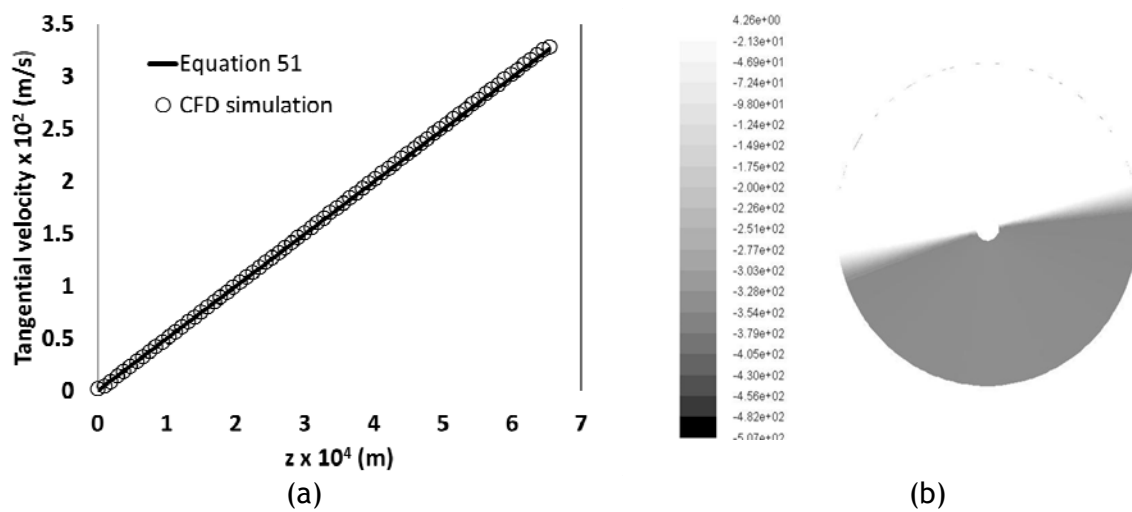
Figure 45 Velocity (a) and pressure map (b) in Pa for ratio 2

Also, the mixing between two fluids with a viscosity ratio of 10 was simulated in Ansys Fluent. Figure 46 shows the results of rotation of the cone after 1.53 s.

Figure 46 Result of the distribution of each fluid after one quarter of the rotation for viscosity ratio 10

As it is possible conclude by observing of Figure 46, the time is too short to have conclusions about the instability of the interface and viscous fingering. Thereby, the comparison carried out in Chapter 4, i.e., the distribution of each lamella for viscosity ratio 1, could correspond or not to the position of each fluid for ratio 10.

In Figure 47 is illustrated the shear stress along the number of rotations. The apparent viscosity decreases, however, it is impossible to observe the increase after half turn as the rheological tests reported.
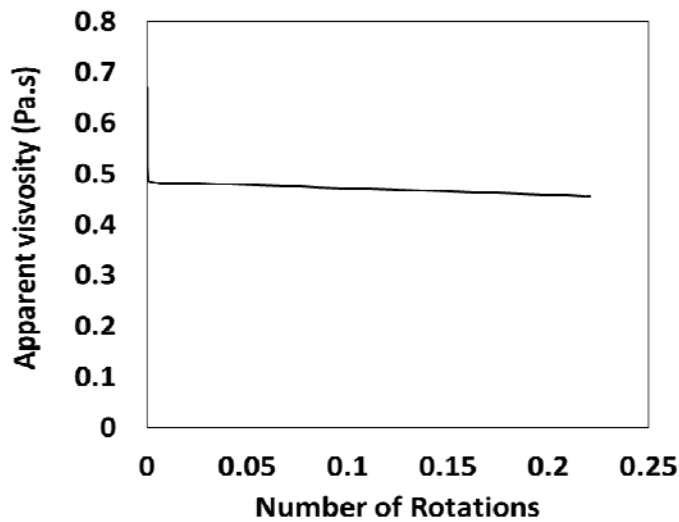
Figure 47 Shear stress in the top wall versus the number of rotations for ratio 10

Figure 48 corresponds to pressure and velocity profiles for the mixing of two fluids with viscosity ratio 10. As in the ratio 2, the velocity profile is given by equation proposed by Macosko (1993) and the pressure is different depending on the fluid.


(a)   (b)
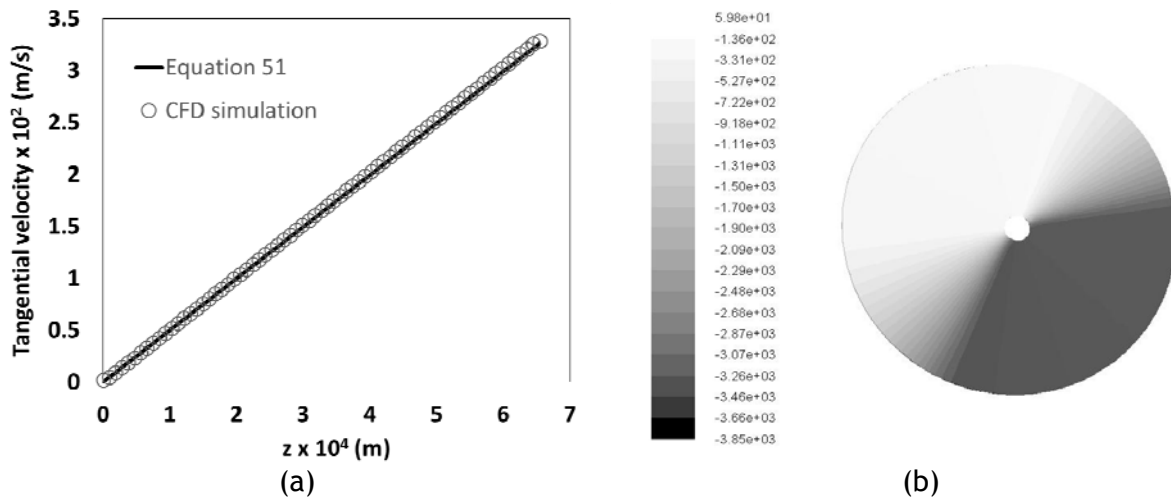
Figure 48 Velocity (a) and pressure map (b) in Pa for ratio 10

For viscosity ratios 2 and 10, as the time required to simulate is high, it is impossible to compare the CFD results and the experimental tests. However, the quality of the simulations was evaluated by the observation of the pressure and velocity profile. Although the pressure field (Figure 45 and Figure 48) presents a difference in relation of the pressure profile in steady state (Figure 37), the velocity profiles are expressed by the equation proposed by Macosko (1993) checking out the validity of solutions.

6 Conclusions

Plate/plate and cone/plate rheometers are devices where the loaded fluid is deformed by shearing and a pure shear of flow is generated creating adjacent layers of fluid which slide over each other with different speeds.

The difference of velocities between the two plates creates a linear velocity profile where the maximum velocity depends of the position from the rotation axis, i.e., the tangential velocity in the top changes with the angular speed and the distance from the center.

When the domain is divided in two similar fluids side-by-side, the induced shear stretches out the interface of the two fluids creating striation thinning laminas. Cross sectional planes, in the normal direction to the top rotation, show the location of two phases inside the cylinder. After two turns, the two fluids form a lamellar structure with two lamellae, having a scale of $s = h/4$, where h is the height of the cylinder for a plate/plate rheometer. On the other side, in cone/plate devices, the scale is given by $s = \beta R_p/4$, where β is the degree defined by cone and plate. The reduction of the mixing scale and the generation of the interfacial area in these devices are completely set by the number of rotations n: $s = h/2n$ for plate/plate geometry and $s = \beta R_p/2n$ for cone/plate system.

Another relative position between the fluids is scrutinized, i.e, two phases are set over each other parallel to the top rotating plate. In this case, the mixing scales and the interface of both phases are kept without any change due to the topology of two phases interface.

Numerical diffusivity is a crucial point in the simulations because its presence causes the simulated system to behave differently than the physical system. However, in this work, the influence of this concept is not estimated.

The mixing of two dissimilar fluids, i.e., substances with different properties, was performed in these devices. In plate/plate rheometer, glycerol and water were set as the working fluids. The difference of viscosity produces a motion between the two species. The glycerol occupies the center dragging the water to the periphery.

The mixing between glycerol and water was performed in a rheometer with a cone/plate geometry. Over time, the apparent viscosity oscillates and the changing of the distribution of each lamellae is a possible reason for this behavior. However, to prove this theory, the experimental conditions were simulated for fluids with a viscosity ratio of 10. But the high time required to simulate this case made it impossible to draw conclusions within the time frame of this work.

6.1 Limitations and Future Work

The main limitation of this thesis was the complexity of the resolution of the Partial Differential Equations (PDEs) that expresses the motion in these devices and mass transfer equation. Maple was the program used to try to solve these equations. The solution obtained was a complex expression and was not possible to get physical meaning of the general solution. However, for the motion equations, this problem was solved through the comparison with the approximated solutions presented by other authors.

On the other side, the major difficulty found was the high time required to simulate the mixing between two fluids with different viscosities in a rheometer using a cone/plate geometry.

In the future, there are some points that could be explored as the case of making kinetic studies with these geometries, for example, a reaction of polymerization. Also, a deep study of the influence of numerical diffusivity, the limitations of the VOF model and the simulation of other viscosity ratios as ratio 4, 100 and 1000 are some situations that could be studied.

7 References

Ansys. 2016. *Fluent Theory Guide*.

Bataineh, Khaled M. 2014. "Numerical investigation of secondary flow effect in cone–plate viscometer." *Computers & Fluids* no. 101:105-113.

Bird, R. Byron, Warren E. Stewart, and Edwin N. Lightfoot. 2007. *Transport phenomena*. Vol. Revised 2nd ed. New York: John Wiley & Sons, Inc.

D'Errico, G., O. Ortona, F. Capuano, and V. Vitagliano. 2004. "Diffusion coefficients for the binary system glycerol plus water at 25 degrees C. A velocity correlation study." *Journal of Chemical and Engineering Data* no. 49 (6):1665-1670. doi: 10.1021/je049917u.

Danckwerts, PV. 1952. "The definition and measurement of some characteristics of mixtures." *Appl. Sci. Res.*

Fields, Steven D., and Julio M. Ottino. 1987. "Effect of striation thickness distribution on the course of an unpremixed polymerization." *Chemical Engineering Science* no. 42 (3):459-465.

Fonte, Cláudio Pereira da. 2012. *Mixing Studies with Impinging Jets PIV/PLIF Experiments and CFD Simulation*, Chemical engineering department, Faculty Engineering of Porto, Porto.

Fonte, Cláudio Pereira da, Ricardo J. Santos, Madalena M. Dias, and José Carlos B. Lopes. 2011. "Quantification of Mixing in RIM using non-diffusive two-phases Flow Numerical Model." *International Journal of Chemical Reactor Engineering* no. 9 (A114).

Laranjeira, P. E. M., José Carlos B. Lopes, and Madalena M. Dias. 2009. "NETmix®, A New Type of Static Mixer: Modeling, Simulation, Macromixing, and Micromixing Characterization." *AiChE Journal* no. 55:2226-2243.

Lopes, J.C.B., P.E.L. Laranjeira, M.M.Q. Dias, and A.A. Martins. 2013. Network Mixer and Related Mixing Process.

Macosko, Christopher W. 1993. *RHEOLOGY Principles, Measurements and Applications*. Minneapolis.

Mohr, W. D., R. L. Saxton, and C. H. Jepson. 1957a. "Mixing in Laminar-Flow Systems." *Industrial and Engineering Chemistry* no. 49 (11):1855-1856. doi: Doi 10.1021/Ie50575a030.

Mohr, W. D., R. L. Saxton, and C. H. Jepson. 1957b. "Theory of Mixing in the Single-Screw Extruder." *Industrial and Engineering Chemistry* no. 49 (11):1857-1862.

Ottino, J M, W E Ranz, and C W Macosko. 1978. "A lamellar model for analysis of liquid-liquid mixing." *Chemical Engineering Science* no. 34:877-890.

Ottino, J. M. 1980. "Lamellar mixing models for structured chemical reactions and their relationship to statistical models; Macro- and micromixing and the problem of averages." *Chemical Engineering Science* no. 35 (6):1377-1381.

Ottino, J. M. 1997. *The kinematics of mixing: stretching, chaos and transport*: Cambridge University Press.

Ottino, Julio M., and Stephen Wiggins. 2004. "Introduction: mixing in microfluidics." *Philosophical transactions of the royal society*.

Ranz, William E. 1979. "Applications of a Stretch Model Diffusion, and Reaction in Laminar and Turbulent Flows." *AIChE Journal* no. 25.

Santos, Ricardo J. 2003. *Mixing Mechanisms in Reaction Injection Moulding - RIM*, Chemical Engineering Department, University of Porto, Porto.

Santos, Ricardo J., Madalena M. Dias, and José Carlos B. Lopes. 2012. *Single and Two-Phase Flows on Chemical and Biomedical Engineering*.

Spencer, R S, and R M Wiley. 1951. *Journal Colloid Science*.

Torres, Marina Verenčević Lima. 2014. *An experimental procedure for Reaction Injection Moulding – RIM – materials formulation design*, Chemical engineering department, Faculty Engineering of Porto, Porto, Porto.

Appendix 1

For Newtonian fluids the shear stress is given by,

$$\zeta_{xz} = -\mu \frac{\partial v_z}{\partial x} \qquad (A.1)$$

When two fluids with different viscosities, I and II, are one over the other as in Figure 49, the velocity profile is different in each case and depends of the position of the interface (x^*), i.e., the thickness of each fluid, and its velocity in the interface(v^*).
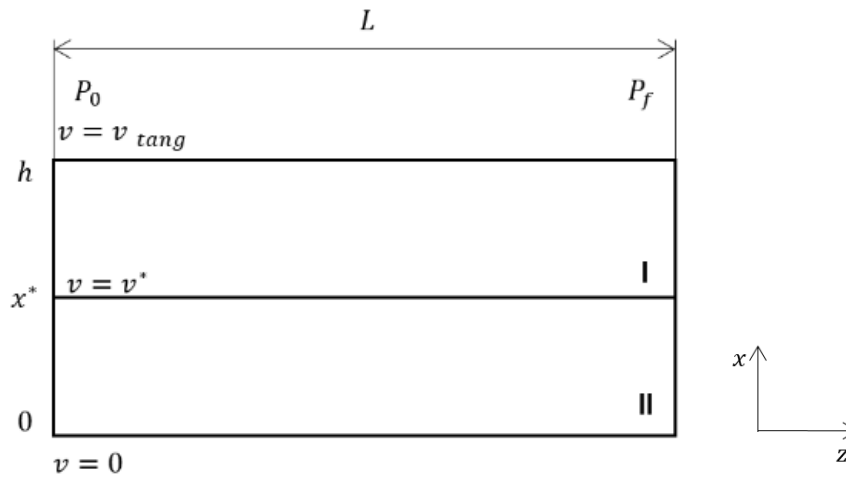

Figure 49 System composed by two lamellae with diferente viscosities

Comparing this case with the flow between two parallel plates (Bird, Stewart, and Lightfoot 2007),

$$\frac{\partial \tau_{xz}}{\partial z} = \frac{\Delta p}{\Delta z} = \frac{p_f - p_0}{L} \qquad (A.2)$$

Considering that Figure 49 is a picture of the distribution of each lamella in outside wall, the difference of pressure p_f and p_0 is zero otherwise there would have discontinuities. Integrating from 0 to x the Equation (A.2) for each fluid, the shear stress is given by,

$$\begin{cases} \tau_{xz}^I = C_1^I \\ \tau_{xz}^{II} = C_1^{II} \end{cases} \qquad (A.3)$$

where τ_{xz}^I and τ_{xz}^{II} are shear stress in each fluid.

When $x = x^*$, $\tau_{xz}^I = \tau_{xz}^{II}$, i.e., at the fluids interface the shear stress exerted on both fluids are equal, then $C_1^I = C_1^{II} = \tau$.

For Newtonian fluids,

$$\begin{cases} -\mu^I \dfrac{\partial v_z{}^I}{\partial x} = \tau \\[2mm] -\mu^{II} \dfrac{\partial v_z{}^{II}}{\partial x} = \tau \end{cases} \tag{A.4}$$

where μ^I is the viscosity of fluid I and μ^{II} is the viscosity of fluid II.

Solving the ODEs,

$$\begin{cases} \partial v_z{}^I = -\dfrac{\tau}{\mu^I}\, \partial x \\[2mm] \partial v_z{}^{II} = -\dfrac{\tau}{\mu^{II}}\, \partial x \end{cases} \leftrightarrow \begin{cases} v^I = -\dfrac{\tau}{\mu^I}\, x + C_2^I \\[2mm] v^{II} = -\dfrac{\tau}{\mu^{II}}\, x + C_2^{II} \end{cases} \tag{A.5}$$

where v^I is the velocity in fluid I and v^{II} is the velocity in fluid II.

Being the boundary conditions of this system,

$$x = 0 \qquad v^{II} = 0 \tag{A.6}$$

$$x = h \qquad v^I = v_{tang} \tag{A.7}$$

$$x = x^* \qquad v^I = v^{II} \tag{A.8}$$

Solving the system,

$$\begin{cases} v^I = \dfrac{1}{\mu^I} \dfrac{v_{tang}}{\dfrac{h}{\mu^I} - \dfrac{x^*}{\mu^I} + \dfrac{x^*}{\mu^{II}}}\, x + \dfrac{v_{tang}}{\dfrac{h}{\mu^I} - \dfrac{x^*}{\mu^I} + \dfrac{x^*}{\mu^{II}}}\, \left(\dfrac{1}{\mu^{II}} + \dfrac{1}{\mu^I}\right) \\[6mm] v^{II} = \dfrac{1}{\mu^{II}} \dfrac{v_{tang}}{\dfrac{h}{\mu^I} - \dfrac{x}{\mu^I} + \dfrac{x}{\mu^{II}}}\, x \end{cases} \tag{A.9}$$

The velocity of the interface (v^*) can be calculated by equation of v^{II} described in Equation A.9,

$$v^* = \dfrac{1}{\mu^{II}} \dfrac{v_{tang}}{\dfrac{h}{\mu^I} - \dfrac{x^*}{\mu^I} + \dfrac{x^*}{\mu^{II}}}\, x^* \tag{A.10}$$

For a system composed by three lamellae, the same reasoning should be done.

Figure 50 illustrates a system composed of three fluids, I, II and III where fluid III is above, following of fluid II and, finally, the fluid I.
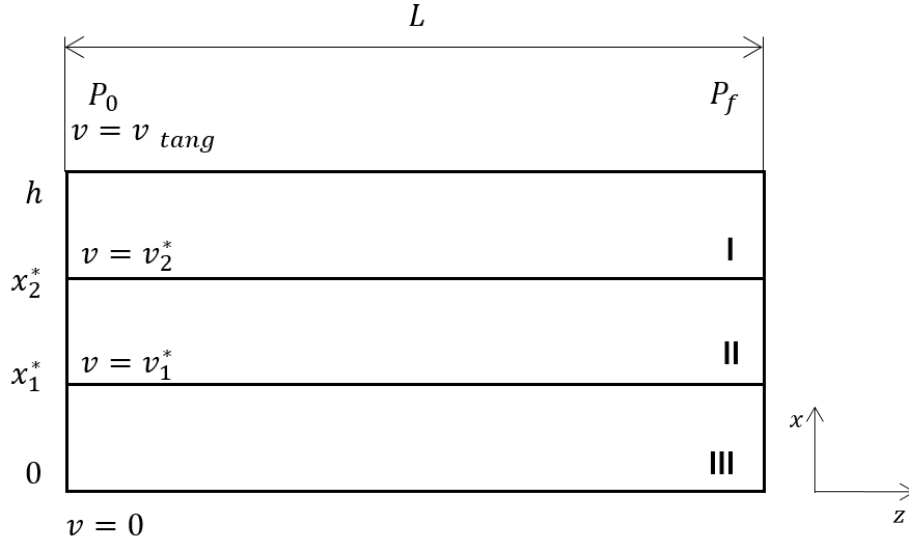

Figure 50 System composed by three lamellas with diferente viscosities

Integrating from 0 to x the Equation (A.2) for each fluid, the shear stress is given by,

$$\begin{cases} \tau_{xz}^I = C_1^I \\ \tau_{xz}^{II} = C_1^{II} \\ \tau_{xz}^{III} = C_1^{III} \end{cases} \tag{A.11}$$

When $x = x^*$, $\tau_{xz}^I = \tau_{xz}^{II} = \tau_{xz}^{III}$, then $C_1^I = C_1^{II} = C_1^{III} = \tau$.

For Newtonian fluids,

$$\begin{cases} -\mu^I \dfrac{\partial v_z{}^I}{\partial x} = \tau \\ -\mu^{II} \dfrac{\partial v_z{}^{II}}{\partial x} = \tau \\ -\mu^{III} \dfrac{\partial v_z{}^{III}}{\partial x} = \tau \end{cases} \tag{A.12}$$

where μ^{III} is the viscosity of the fluid III.

Solving the system of ODEs,

$$\begin{cases} \partial v_z{}^I = -\dfrac{\tau}{\mu^I}\,\partial x \\[2mm] \partial v_z{}^{II} = -\dfrac{\tau}{\mu^{II}}\,\partial x \\[2mm] \partial v_z{}^{III} = -\dfrac{\tau}{\mu^{III}}\,\partial x \end{cases} \leftrightarrow \begin{cases} v^I = -\dfrac{\tau}{\mu^I}\,x + C_2^I \\[2mm] v^{II} = -\dfrac{\tau}{\mu^{II}}\,x + C_2^{II} \\[2mm] v^{III} = -\dfrac{\tau}{\mu^{III}}\,x + C_2^{III} \end{cases} \tag{A.13}$$

Being boundary conditions,

$$x = 0 \qquad v^{III} = 0 \tag{A.14}$$

$$x = h \qquad v^I = v_{tang} \tag{A.15}$$

$$x = x_2^* \qquad v^I = v^{II} \tag{A.16}$$

$$x = x_1^* \qquad v^{III} = v^{II} \tag{A.17}$$

Solving the system,

$$\begin{cases} v^I = \dfrac{v_{tang}}{\dfrac{h}{\mu^I} + \dfrac{x_2^*}{\mu^{II}} - \dfrac{x_2^*}{\mu^I} + \dfrac{x_1^*}{\mu^{III}} - \dfrac{x_1^*}{\mu^{II}}}\left(\dfrac{x}{\mu^I} + \dfrac{x_2^*}{\mu^{II}} - \dfrac{x_2^*}{\mu^I} + \dfrac{x_1^*}{\mu^{III}} - \dfrac{x_1^*}{\mu^{II}}\right) \\[6mm] v^{II} = \dfrac{v_{tang}}{\dfrac{h}{\mu^I} + \dfrac{x_2^*}{\mu^{II}} - \dfrac{x_2^*}{\mu^I} + \dfrac{x_1^*}{\mu^{III}} - \dfrac{x_1^*}{\mu^{II}}}\left(\dfrac{x}{\mu^{II}} + \dfrac{x_1^*}{\mu^{III}} - \dfrac{x_1^*}{\mu^{II}}\right) \\[6mm] v^{III} = \dfrac{1}{\mu^{III}}\dfrac{v_{tang}}{\dfrac{h}{\mu^I} + \dfrac{x_2^*}{\mu^{II}} - \dfrac{x_2^*}{\mu^I} + \dfrac{x_1^*}{\mu^{III}} - \dfrac{x_1^*}{\mu^{II}}}\,x \end{cases} \tag{A.18}$$

The velocity of the interface between the fluid III and II (v_1^*) can be calculated by equation of v^{III} described in Equation A.18,

$$v_1^* = \dfrac{1}{\mu^{III}}\dfrac{v_{tang}}{\dfrac{h}{\mu^I} + \dfrac{x_2^*}{\mu^{II}} - \dfrac{x_2^*}{\mu^I} + \dfrac{x_1^*}{\mu^{III}} - \dfrac{x_1^*}{\mu^{II}}}\,x_1^* \tag{A.19}$$

On the order hand, the velocity of the interface between the fluid II and I (v_2^*) can be calculated by equation of v^{II} described in Equation A.18,

$$v_2^* = \dfrac{v_{tang}}{\dfrac{h}{\mu^I} + \dfrac{x_2^*}{\mu^{II}} - \dfrac{x_2^*}{\mu^I} + \dfrac{x_1^*}{\mu^{III}} - \dfrac{x_1^*}{\mu^{II}}}\left(\dfrac{x_2^*}{\mu^{II}} + \dfrac{x_1^*}{\mu^{III}} - \dfrac{x_1^*}{\mu^{II}}\right) \tag{A.20}$$

The system illustrated in Figure 51 is composed by four lamellae that consists of fluids I, II, III and IV being fluid IV below and fluid I above.
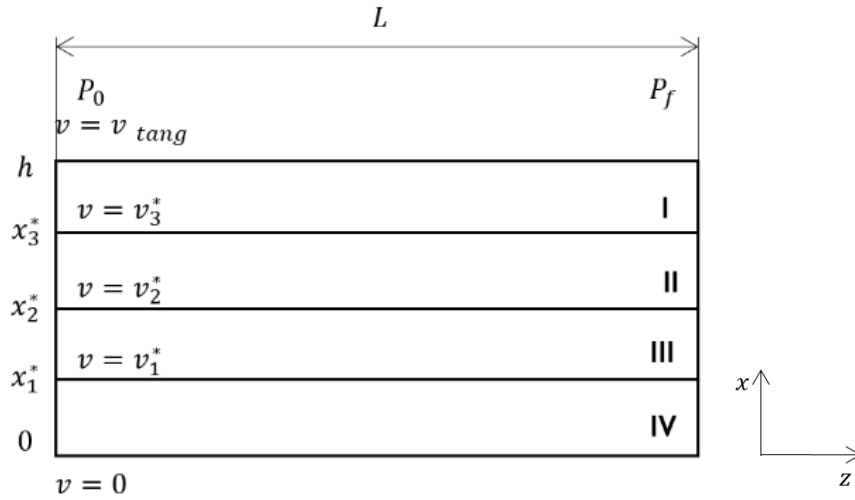

Figure 51 System composed by four lamellas with diferente viscosities

Integrating from 0 to x the Equation (A.2) for each fluid, the shear stress is given by,

$$\begin{cases} \tau_{xz}^I = C_1^I \\ \tau_{xz}^{II} = C_1^{II} \\ \tau_{xz}^{III} = C_1^{III} \\ \tau_{xz}^{IV} = C_1^{IV} \end{cases} \tag{A.21}$$

when $x = x^*$, $\tau_{xz}^I = \tau_{xz}^{II} = \tau_{xz}^{III} = \tau_{xz}^{IV}$, then $C_1^I = C_1^{II} = C_1^{III} = C_1^{IV} = \tau$.

For Newtonian fluids,

$$\begin{cases} -\mu^I \dfrac{\partial v_z^{\,I}}{\partial x} = \tau \\[2mm] -\mu^{II} \dfrac{\partial v_z^{\,II}}{\partial x} = \tau \\[2mm] -\mu^{III} \dfrac{\partial v_z^{\,III}}{\partial x} = \tau \\[2mm] -\mu^{IV} \dfrac{\partial v_z^{\,IV}}{\partial x} = \tau \end{cases} \tag{A.22}$$

where μ^{IV} is the viscosity of the fluid IV.

Solving the system of ODEs,

$$\begin{cases} \partial v_z{}^I = -\dfrac{\tau}{\mu^I}\,\partial x \\[2mm] \partial v_z{}^{II} = -\dfrac{\tau}{\mu^{II}}\,\partial x \\[2mm] \partial v_z{}^{III} = -\dfrac{\tau}{\mu^{III}}\,\partial x \\[2mm] \partial v_z{}^{IV} = -\dfrac{\tau}{\mu^{IV}}\,\partial x \end{cases} \leftrightarrow \begin{cases} v^I = -\dfrac{\tau}{\mu^I}\,x + C_2^I \\[2mm] v^{II} = -\dfrac{\tau}{\mu^{II}}\,x + C_2^{II} \\[2mm] v^{III} = -\dfrac{\tau}{\mu^{III}}\,x + C_2^{III} \\[2mm] v^{IV} = -\dfrac{\tau}{\mu^{IV}}\,x + C_2^{IV} \end{cases} \qquad (A.23)$$

The boundary conditions are

$$x = 0 \qquad v^{IV} = 0 \qquad\qquad (A.24)$$

$$x = h \qquad v^I = v_{tang} \qquad\qquad (A.25)$$

$$x = x_1^* \qquad v^{IV} = v^{II)} \qquad\qquad (A.26)$$

$$x = x_2^* \qquad v^{III} = v^{II} \qquad\qquad (A.27)$$

$$x = x_3^* \qquad v^I = v^{II} \qquad\qquad (A.28)$$

Solving the system,

$$\begin{cases} v^I = \dfrac{v_{tang}}{\dfrac{h}{\mu^I} + \dfrac{x_3^*}{\mu^{II}} - \dfrac{x_3^*}{\mu^I} + \dfrac{x_2^*}{\mu^{III}} - \dfrac{x_2^*}{\mu^{II}} + \dfrac{x_1^*}{\mu^{IV}} - \dfrac{x_1^*}{\mu^{III}}}\left(\dfrac{x}{\mu^I} + \dfrac{x_3^*}{\mu^{II}} - \dfrac{x_3^*}{\mu^I} + \dfrac{x_2^*}{\mu^{III}} - \dfrac{x_2^*}{\mu^{II}} + \dfrac{x_1^*}{\mu^{IV}} - \dfrac{x_1^*}{\mu^{II}}\right) \\[6mm] v^{II} = \dfrac{v_{tang}}{\dfrac{h}{\mu^I} + \dfrac{x_3^*}{\mu^{II}} - \dfrac{x_3^*}{\mu^I} + \dfrac{x_2^*}{\mu^{III}} - \dfrac{x_2^*}{\mu^{II}} + \dfrac{x_1^*}{\mu^{IV}} - \dfrac{x_1^*}{\mu^{III}}}\left(\dfrac{x}{\mu^{II}} + \dfrac{x_2^*}{\mu^{III}} - \dfrac{x_2^*}{\mu^{II}} + \dfrac{x_1^*}{\mu^{IV}} - \dfrac{x_1^*}{\mu^{II}}\right) \\[6mm] v^{III} = \dfrac{v_{tang}}{\dfrac{h}{\mu^I} + \dfrac{x_3^*}{\mu^{II}} - \dfrac{x_3^*}{\mu^I} + \dfrac{x_2^*}{\mu^{III}} - \dfrac{x_2^*}{\mu^{II}} + \dfrac{x_1^*}{\mu^{IV}} - \dfrac{x_1^*}{\mu^{III}}}\left(\dfrac{x}{\mu^{III}} + \dfrac{x_1^*}{\mu^{IV}} - \dfrac{x_1^*}{\mu^{III}}\right) \\[6mm] v^{IV} = \dfrac{1}{\mu^{IV}}\dfrac{v_{tang}}{\dfrac{h}{\mu^I} + \dfrac{x_3^*}{\mu^{II}} - \dfrac{x_3^*}{\mu^I} + \dfrac{x_2^*}{\mu^{III}} - \dfrac{x_2^*}{\mu^{II}} + \dfrac{x_1^*}{\mu^{IV}} - \dfrac{x_1^*}{\mu^{III}}}\,x \end{cases} \qquad (A.29)$$

The velocity of the interface between the fluid IV and III (v_1^*) can be calculated by equation of v^{IV} described in Equation A.30,

$$v_1^* = \dfrac{1}{\mu^{IV}}\dfrac{v_{tang}}{\dfrac{h}{\mu^I} + \dfrac{x_3^*}{\mu^{II}} - \dfrac{x_3^*}{\mu^I} + \dfrac{x_2^*}{\mu^{III}} - \dfrac{x_2^*}{\mu^{II}} + \dfrac{x_1^*}{\mu^{IV}} - \dfrac{x_1^*}{\mu^{III}}}\,x_1^* \qquad (A.30)$$

On the order hand, the velocity of the interface between the fluid III and II (v_2^*) can be calculated by equation of v^{III} described in Equation A.30,

$$v_2^* = \dfrac{v_{tang}}{\dfrac{h}{\mu^I} + \dfrac{x_3^*}{\mu^{II}} - \dfrac{x_3^*}{\mu^I} + \dfrac{x_2^*}{\mu^{III}} - \dfrac{x_2^*}{\mu^{II}} + \dfrac{x_1^*}{\mu^{IV}} - \dfrac{x_1^*}{\mu^{III}}}\left(\dfrac{x_2^*}{\mu^{III}} + \dfrac{x_1^*}{\mu^{IV}} - \dfrac{x_1^*}{\mu^{III}}\right) \qquad (A.31)$$

Finally, the velocity of the interface between the fluid II and I (v_3^*) can be calculated by equation of v^{II} described in Equation A.30,

$$v_3^* = \frac{v_{tang}}{\frac{h}{\mu^I} + \frac{x_3^*}{\mu^{II}} - \frac{x_3^*}{\mu^I} + \frac{x_2^*}{\mu^{III}} - \frac{x_2^*}{\mu^{II}} + \frac{x_1^*}{\mu^{IV}} - \frac{x_1^*}{\mu^{III}}} \left(\frac{x_3^*}{\mu^{II}} + \frac{x_2^*}{\mu^{III}} - \frac{x_2^*}{\mu^{II}} + \frac{x_1^*}{\mu^{IV}} - \frac{x_1^*}{\mu^{II}} \right) \tag{A.32}$$